UNIVERSITY OF CALIFORNIA, SAN DIEGO

Influence of Soil Permeability on Liquefaction-Induced Lateral Pile Response

A thesis submitted in partial satisfaction of the requirements

for the Degree of Master of Science

in

Structural Engineering

by

Jose Manuel Ramirez

Committee in charge:

Professor Ahmed Elgamal, Chair
Professor Tara Hutchinson
Professor Benson Shing

2010

The Thesis of Jose Manuel Ramirez is approved and it is acceptable in quality and form for publication on microfilm and electronically:

_____

_____

_____

Chair

University of California, San Diego

2010

DEDICATION

To my parents Jose and Josefina and all my family and friends who supported me.

TABLE OF CONTENTS

LIST OF FIGURES

LIST OF TABLES

ACKNOWLEDGEMENTS

First and foremost, I would like to express my most sincere and deepest appreciation to my advisor, Professor Ahmed Elgamal for giving me the opportunity to pursue my M.S. Thesis degree under his guidance. His rigorous teachings and sincere concern for my education have been encouraging and motivational. I am eternally grateful for having him as my advisor and mentor and for all his valuable academic and professional support.

I also would like to specially thank Dr. Jinchi Lu for his unconditional assistance in conducting this computational analysis research. His time, dedication, and input have been extremely valuable and are greatly appreciated.

I am grateful to Dr. Liangcai He for setting up the framework that made my research possible and for allowing me to take advantage of his computational resources, which made my research flow much smoother.

This research was supported by the National Science Foundation (award number CMS-052995) and the Pacific Earthquake Engineering Research Center (PEER), Lifelines Program. The mildly inclined laminar container testing-configuration is patterned after the earlier centrifuge research effort of Rensselaer Polytechnic Institute (Professors Ricardo Dobry and Tarek Abdoun). Under the oversight of Professor Tokimatsu, the experiments using the large laminar container were conducted at the National Research Institute for Earth Science and Disaster

Prevention (NIED) laboratory in Tsukuba, Japan (Dr. Akio Abe, Dr. Masayoshi Sato, and Professor Kohji Tokimatsu).

ABSTRACT OF THE THESIS

Influence of Soil Permeability on Liquefaction-Induced Lateral Pile Response

by

Jose Manuel Ramirez

Master of Science in Structural Engineering

University of California, San Diego, 2010

Professor Ahmed Elgamal, Chair

Pile foundations have been significantly damaged by liquefaction-induced lateral spreading during earthquakes. There are large uncertainties regarding the effects of various soil properties on this pattern of soil-structure interaction. The main concern of this study is to *numerically* investigate the role of soil permeability in such lateral spreading scenarios.

Through extensive calibration, finite element analysis models were developed in which the response reasonably matched experimental data from shake-table testing and centrifuge testing. The overall impact of permeability on the soil stratum and the pile response was similar for both situations. In most cases, soil displacement increased with increasing permeability, while pile load decreased.

CHAPTER 1

OUTLINE

1.1 Research Background

In view of past earthquake observations, researchers have been interested in the problem of liquefaction-induced lateral spreading and its effects on pile foundations. Experimental studies have been a main tool to gain insights. He (2005) documented earlier efforts related to this large domain of research investigations.

Two main experimental techniques will be the basis for numerical studies conducted herein, namely:

1. Shake-table testing, particularly from research conducted at the NIED facility in Tsukuba, Japan, and
2. Centrifuge testing, particularly from research conducted at Rensselaer Polytechnic Institute, Troy, NY, USA.

Data from experiments at these facilities will be used herein to calibrate a representative computational model. The model will then be used to look at the impact of soil permeability on the soil stratum, and on the pile loads. As such, this may be viewed as an attempt to extend the experimental sand permeability data insights to other significant practical scenarios of liquefaction in the range of silt and gravel permeability.

1.2 Thesis Outline

Chapter 2 describes numerical modeling effort and presents the main findings from the entire research effort. Chapter 3 presents additional investigations for a sand model with dilative properties. Appendices include additional figures to complement the concise presentations of Chapter 2 and Chapter 3. Finally, Chapter 4 is a brief summary along with main finding highlights.

CHAPTER 2

INFLUENCE OF SOIL PERMEABILITY ON LIQUEFACTION- INDUCED LATERAL PILE RESPONSE

2.1 Abstract

A three-dimensional nonlinear dynamic finite element analysis was conducted to simulate shake-table tests on piles subjected to liquefaction induced lateral spreading. The simulation employs a solid-fluid fully coupled formulation and a soil constitutive model based on a multi-surface plasticity framework. Upon calibration, the finite element analysis has produced a model response that reasonably matched the shake-table data. It was observed that as soil permeability increased, soil displacement increased, while the lateral load on the piles generally decreased. It was also observed that very high permeability values weaken the effect of soil dilation precluding high excess pore pressure build up and resulting in a decrease in pile load and soil displacement.

2.2 Introduction

In the following sections, a brief description of the experiment is first presented. Subsequently, the employed FE analysis framework and soil constitutive model are described. The finite element model and model parameters are then highlighted. Finally, results of the FE simulations are presented and discussed. Aspects of model response, including pore pressure buildup, soil lateral deformation and pile displacement, are examined.

2.3 Shake-table Test

The experiment simulated in this study is Japan4 reported in He (2005). As indicated in Figure 2.1, the employed laminar box is about 12 m long, 6 m high and 3.5 m wide. The container and ground surface were inclined at 2º to the horizontal, patterned after Abdoun *et al.* (2003) and Dobry *et al.* (2003), to simulate pile response in a mild infinite slope situation. The input motion was sinusoidal with a dominant frequency of about 2 Hz and amplitude of about 0.2 g. A picture of the soil laminar box before testing is shown in Figure 2.2.

The sand stratum in this model was constructed by the sedimentation method (sand deposition in water) and the entire sand layer was submerged. Relative density was about 40-50%, and saturated density was about 1940 kg/m^3. The model was instrumented with accelerometers and pore pressure sensors within the soil stratum.

In the experiment, before construction of the soil stratum, steel piles (Figure 2.3) were connected to the base in an attempt to achieve a fixed base condition. Both piles had a 0.318 m diameter but the stiff pile had a 6 mm wall thickness while the flexible pile had a 3 mm wall thickness. Before soil layer construction, static pushover tests were conducted on each pile to obtain the bending stiffness EI and the actual rotational base stiffness. Each pile was also densely instrumented as depicted in Figure 2.1, of which more important for this study were the displacement transducers available at the pile head.

Displacement transducers were mounted on the laminar box exterior wall to measure free-field lateral displacement. The completed experimental model consisted of a single layer of saturated sand with a thickness of 5.0 m. With the container in this

inclined configuration, the piles were installed vertically. As such, Japan4 included two separate single piles with different stiffness properties (He 2005, He *et al.* 2006). Figure 2.4 shows 1 m of lateral spreading of the laminar box.

2.4 Numerical Modeling

2.4.1 Finite Element Analysis Framework

Modeling and computations are performed using the PEER (Pacific Earthquake Engineering Research Center) finite element analysis framework, OpenSees (Open System for Earthquake Engineering Simulation). OpenSees is an open source, object-oriented nonlinear finite element analysis framework for simulating seismic response of structural and geotechnical systems (http://opensees.berkeley.edu).

The object-oriented software design philosophy of OpenSees allows the integration of existing libraries and new components into the framework without modifying the existing code. This feature makes it relatively easy to add new components into the framework. Accordingly, the capabilities of OpenSees are growing rapidly. The current version of OpenSees includes an extensive library of material constitutive models and finite elements as well as equation solvers, time integration schemes, and solution algorithms.

The OpenSees framework consists of a modeling module and an analysis module. The modeling module develops the finite element model components, such as nodes, elements, materials, loads and constraints. The analysis module specifies an analysis procedure (including equation solvers, time integration schemes, and solution

algorithms), selection of quantities to be monitored during the analysis, and the output of results.

2.4.2 Soil Constitutive Model

Satisfactory modeling of the experiment hinged on a soil constitutive model (Figures 2.5 and 2.6) that has been implemented in OpenSees by Yang *et al.* (2003) http://cyclic.ucsd.edu/opensees. This model is capable of representing the salient characteristics of soil liquefaction and associated accumulation of shear deformations (Parra 1996, Yang 2000, Elgamal *et al.* 2003, Yang *et al.* 2003, Yang and Elgamal 2003).

In this model, special attention is placed on controlling the magnitude of liquefaction-induced cycle-by-cycle shear strain accumulation in clean medium-dense sands (Parra 1996, Yang 2000, Elgamal *et al.* 2003, Yang *et al.* 2003). The experimentally observed accumulation of permanent deviatoric strain is modeled as a distinct phase, within the framework of multi-surface plasticity (Prevost 1985). In this multi-surface plasticity framework, a number of similar conical yield surfaces (20 herein) with different tangent shear moduli are employed to represent shear stress-strain nonlinearity and the confinement dependence of shear stiffness and shear strength. Furthermore, appropriate loading-unloading flow rules are devised to reproduce the strong dilative tendency, which results in increased shear stiffness and strength (at large cyclic shear strain excursions). The main components of this model are briefly summarized below. Details about the model can be found from related references (Parra 1996, Yang 2000, Elgamal *et al.* 2003, Yang *et al.* 2003).

The yield function of the model follows the classical plasticity convention (Hill 1950). It is assumed that material elasticity is linear and isotropic, and that nonlinearity and anisotropy result from plasticity. The selected yield function forms a conical surface in stress space with its apex (at - p_0') on the hydrostatic axis (Figure 2.5). In the context of multi-surface plasticity (Iwan 1967, Mroz 1967, Prevost 1985), a number of similar yield surfaces with a common apex and different sizes form the hardening zone (Figure 2.5). The outermost surface is the envelope of peak shear strength (failure envelope).

During shear loading, the soil contractive/dilative behavior is handled by a nonassociative flow rule (Parra 1996, Yang 2000, Elgamal *et al.* 2003, Yang *et al.* 2003) so as to achieve appropriate coupling between shear and volumetric response in accordance with experimental observation. In particular, nonassociativity is restricted to the volumetric component of the plastic flow tensor (outer normal to the plastic potential surface in stress-space). Therefore, depending on the relative location of the stress state (Figure 2.6) with respect to the phase transformation (PT) surface (Ishihara 1985; Vaid and Thomas 1995, Vaid and Sivathayalan 1999; Kramer 1996; Iai 1991; Dobry and Abdoun 1998), distinctive contractive/dilative behaviors are reproduced by specifying appropriate expressions for the nonassociativity condition (Parra 1996, Yang 2000, Elgamal *et al.* 2003, Yang *et al.* 2003, Figure 2.6). Finally, a purely deviatoric kinematic hardening rule (Elgamal *et al.* 2003) is employed in the constitutive model.

In summary, the main modeling parameters include typical dynamic soil properties such as low-strain shear modulus and friction angle, as well as calibration

constants to control pore-pressure buildup rate, dilative tendency, and the level of liquefaction-induced cyclic shear strain. The model has been extensively calibrated (Parra 1996, Yang 2000, Elgamal *et al.* 2003, Yang *et al.* 2003) for clean Nevada sand with a relative density D_r of about 40%. The calibration phase includes results of monotonic and cyclic laboratory tests (Arulmoli *et al.* 1992), as well as data from dynamic centrifuge-model simulations on level ground and infinite mild sloping ground (Taboada 1995, Dobry *et al.* 1995).

2.4.3 Finite Element Model

As described below, the original FE Model was developed by He (2005). Taking advantage of symmetry, only half of the domain is meshed for the 3D FEM study. Figure 2.7 shows the mesh used for the simulation. It is generated and visualized using the pre and post processor software GID (http://gid.cimne.upc.es).

Various types of finite elements are used to represent the pile-soil system. Specifically, the solid-fluid fully coupled 3D 8-8 node elements (brickUP) were used to model the saturated soil. (Parra 1996, Yang 2000, Elgamal *et al.* 2003, Yang *et al.* 2003). This element (Figure 2.8) is a hexahedral linear isoparametric element, based on the Biot (1962) theory of porous materials. It has been implemented by Dr. Zhaohui Yang (University of California, San Diego) in OpenSees for simulating dynamic response of solid-fluid fully coupled material (http://cyclic.ucsd.edu/OpenSees). Each node has 4 degrees-of-freedom (DOF), of which DOFs 1 to 3 are for solid displacement (u) and DOF 4 is for fluid pressure (p).

3D nonlinear beam-column elements (nonlinearBeamColumn) are used to model the two piles. The bending stiffness EI of the piles were 14,320 kN·m^2 for the stiff pile and 7,360 kN·m^2 for the flexible pile. The base spring constants K_r of the piles were rotational springs with constant stiffness 18,500 kN·m/rad and 8,500 kN·m/rad for the stiff pile and flexible pile respectively. The employed nonlinear moment curvature relationships of the piles are shown in Figure 2.9.

Quasi-rigid beam elements, normal to the longitudinal axis of the pile, were used to model the actual size of the cross section of the pile. These quasi-rigid elements are actually elasticBeamColumn elements with rigidity 1000 times larger than the pile rigidity. One end of the quasi-rigid beam elements is connected to the pile and the other end is tied to the concurrent soil node through equal DOF constraints (equalDOF) which impose the same DOF in given directions for any two nodes. Zero length elements (zeroLength) are used to model the fixity condition at the pile base (rotation spring). No special elements were used for the pile-soil interface since the soil constitutive model itself could handle the interface interaction.

The model size is relatively large, having 3085 nodes (Figure 2.7). It is composed of 2240 brickUP elements for the saturated soil, 22 nonlinearBeamColumn elements for the two piles each with 11 elements, two zeroLength elements for the base fixity condition of the two piles, and 100 quasi rigid beam elements for the actual size of the pile cross section. A special sparse equation solver is used to solve the system of equations of the simulation. The sparse solver was developed by Mackay (1992) and Law and Mackay (1993) and implemented in OpenSees by Peng (2002). The solver is based on a row-oriented storage scheme that takes full advantage of the

spare characteristics of the stiffness matrix (Peng 2002) to allow in-core execution for models requiring large computer memory.

Boundary conditions imposed on the model are as follows (He 2005):

(1) The nodes on the plane of symmetry and on the container far side do not displace normal to the plane of symmetry,

(2) The nodes having same distance from the base on the vertical planes on the left and right boundaries are tied to each other (shear beam condition).

(3) The nodes at the bottom of the mesh are fixed except for the lateral shaking direction.

(4) The pore pressure DOF of the nodes at ground surface is fixed (zero fluid pressure).

(5) All peripheral boundaries are impervious.

2.4.4 Model Parameters

Because a newer version of OpenSees was employed, version 2.0.0, the original FE Model had to be recalibrated. After a considerable time-consuming effort in recalibration, the parameters employed in the 3D finite element model case that produced a reasonable match with the experimental data are summarized on Table 2.1, making it the benchmark case. It is important to note that specification of relatively low viscous damping was necessary (Liangcai 2005) in order to reduce the level of acceleration upon liquefaction of the soil stratum. These parameters (Table 2.1) were used in subsequent runs in which only the soil permeability was changed.

Table 2.1. Model parameters employed in the 3D analysis
(PressureDependMultiYield model in OpenSees)

	Parameter	Value
Soil Constitutive Model Parameters	Saturated mass density (g/cm^3)	1.97
	Poisson's ratio ν	0.4
	Reference Shear Modulus (kPa)	33278
	Reference Bulk Modulus (kPa)	155300
	Reference Bulk Modulus for Dynamics (kPa)	22185
	Friction angle ϕ (º)	28
	Peak Shear Strain	0.1
	Reference Pressure (kPa)	80
	Pressure Dependence Coefficient	0.5
	Phase Transformation angle ϕ_T (º)	Deactivated (82)
	Contraction 1	0.3
	Dilation 1	Deactivated
	Dilation 2	Deactivated
	Liquefaction1	0
	Liquefaction2	0
	Liquefaction3	0
	Permeability (m/s)	5.0×10^{-5}
	Numerical Constant for Cohesion (kPa)	0.3
Dynamic FE Analysis Parameters	Gamma (Newmark integration parameter)	0.6
	Beta (Newmark integration parameter)	0.325
	Mass Proportional Damping	0
	Initial Stiffness Proportional Damping	0.002
	Density Multiplier	1.14
	Inclination (degrees)	3
	Fluid-solid combined bulk modulus (kPa)	2200000

2.5 FE Analysis Results

It was a challenging task to produce a close match between the extensive experimental data set (Figure 2.1) and the numerical results. After achieving a reasonable match that focused on overall container and pile displacements and free-field excess pore pressure, the effects of changing soil permeability were explored.

2.5.1 Benchmark Case

As the experiment shows that liquefaction occurred in the first few seconds of shaking and maximum pile response occurred upon liquefaction, only ten seconds of shaking was carried out in the numerical simulation (He 2005). Figure 2.10 shows a comparison between the experimental data and the benchmark case of the overall container displacements at different depths, while Figure 2.11 shows a comparison between the experimental data and the benchmark case of the free-field displacement profile at 10 seconds of shaking. Figure 2.12 shows the pile head displacements. Figure 2.13 shows a comparison between the experimental data and the benchmark case of the free-field excess pore pressure time histories at different depths. Relatively close agreement was observed in all of these figures except for the free-field excess pore pressure time history at a 4.5 m depth in which the experimental lagged at the beginning. Figure 2.14 shows the acceleration time histories for the experimental data in comparison to the benchmark case as well.

2.5.2 Effects of Changing Permeability

In an attempt to explore the effects of changing soil permeability, other numerical analyses were conducted with the parameters described in Table 1, in which only the permeability was changed. The most significant cases that were studied, aside from the benchmark case were the ones in which the permeability was greater than that of the benchmark case, namely with permeability, k, being $5.0x10^{-4}$ m/s, $5.0x10^{-3}$ m/s, and $5.0x10^{-2}$ m/s. Cases with permeability lower than that of the benchmark case were also studied but they followed the general trend observed in the benchmark case.

Figure 2.15 shows the free-field displacement time histories for the four permeability cases mentioned above. It is observed that the cases with higher permeability cause the soil to displace the most except for the case in where the permeability was the highest, $5.0x10^{-2}$ m/s, which showed the least displacement. Also, it is observed that for depths of 2.5 m and greater, the case with the next highest permeability, $5.0x10^{-3}$ m/s also displaced less than the cases with lower permeability. At a 4.5 m depth, in the earlier portion of the time interval, the case with permeability of $5.0x10^{-4}$ m/s showed slightly less displacement than the benchmark case matching it during the latter portion of the time interval. This is reinforced and made more apparent with Figure 2.16, which shows the free-field displacement profile at 10 seconds of shaking for the four permeability cases.

Figure 2.17 shows the variation in flexible and stiff pile head displacements due to the four different permeability cases. Overall, the pile head displacement seems to decrease with increasing permeability. The only exception is on the flexible pile for

the case where the permeability is $5.0x10^{-3}$ m/s in which the head displacement is slightly less than the benchmark at the beginning of the shaking, matches the head displacement of benchmark for a couple of seconds in the middle of the shaking, and then displaces slightly less than the benchmark in the later portion of the shaking.

Figure 2.18 compares the free-field excess pore pressure time histories for the four different permeability cases. It is observed that the soil case with the highest permeability, namely $5.0x10^{-2}$ m/s, did not liquefy. Also, it is observed that the pore pressure build up was less for higher permeability cases than that of the benchmark case, only to be more apparent at greater depths.

Figure 2.19 and Figure 2.20 compare the pore pressure time histories near the stiff pile, on the upslope side and downslope side respectively, for the different permeability cases at different depths. It is observed that cycle-by-cycle dilation is reduced with increasing permeability and that the soil case with the highest permeability did not reach liquefaction.

Similarly, Figure 2.21 and Figure 2.22 compare the pore pressure time histories near the flexible pile, on the upslope side and downslope side respectively, for the different permeability cases at different depths. The observations are similar, only more subtle, that those from the stiff pile. Dilation is reduced with increasing permeability, and the soil case with the highest permeability did not liquefy.

2.6 Discussion

The increase in soil displacement with increasing permeability was observed as a general trend. The exceptions were for the soil case with higher permeability,

$5.0x10^{-2}$ m/s, where the overall displacement was significantly less than that of the benchmark case and for the next highest soil permeability case, $5.0x10^{-3}$ m/s, where the displacements at depths 2.0 m and greater were exceeded by the soil cases with lower permeability. This is more apparent on the free-field displacement profile at 10 seconds, Figure 2.16.

The exceptions to this trend can be explained by the effect increasing permeability has in excess pore pressure build up. An increase in permeability that corresponds to the soil case with a permeability of $5.0x10^{-3}$ m/s starts showing a reduction in pore pressure buildup that is more apparent with depth (Figure 2.18). For the case with the highest permeability, $5.0x10^{-2}$ m/s, the excess pore pressure build is so small that the soil does not liquefy. This reduction in pore pressure buildup or lack of pore pressure buildup serves to maintain the effective soil confinement and most importantly, explains the effect higher permeability has on soil's free-field lateral displacement.

The increase in free-field soil displacement can also be attributed to the effect increasing permeability has on soil dilation. Figure 2.18 shows how increasing soil permeability results in weaker dilation effects. This effect leads to the observed behavior because the suction pressure that kept soil particles together is reduced, allowing the soil to displace more freely.

Similarly, the decrease in pile head displacement with increase in permeability was observed as a general trend (Figure 2.17). As previously mentioned, the increase in permeability results in weaker dilation effects allowing particles to displace more

freely. The soil is able to displace and go around the pile without dragging the pile, which in turn allows for less pile displacement.

2.7 Summary and Conclusions

In summary, it was observed that higher permeability weakens the effect of soil dilation, eventually precluding much excess pore pressure buildup as permeability increases. The main findings from the analyses are summarized as follows:

1. Upon calibration, the finite element analysis produced a reasonable match of pile and soil displacements compared to the experimental measurements.

2. It was found that increasing soil permeability weakens soil dilation and that pile load is reduced while soil displacement is increased. However, it is worthy to note that if the permeability becomes too high, pore pressure buildup is significantly reduced, allowing for soil to displace less, which is more apparent at greater depths.

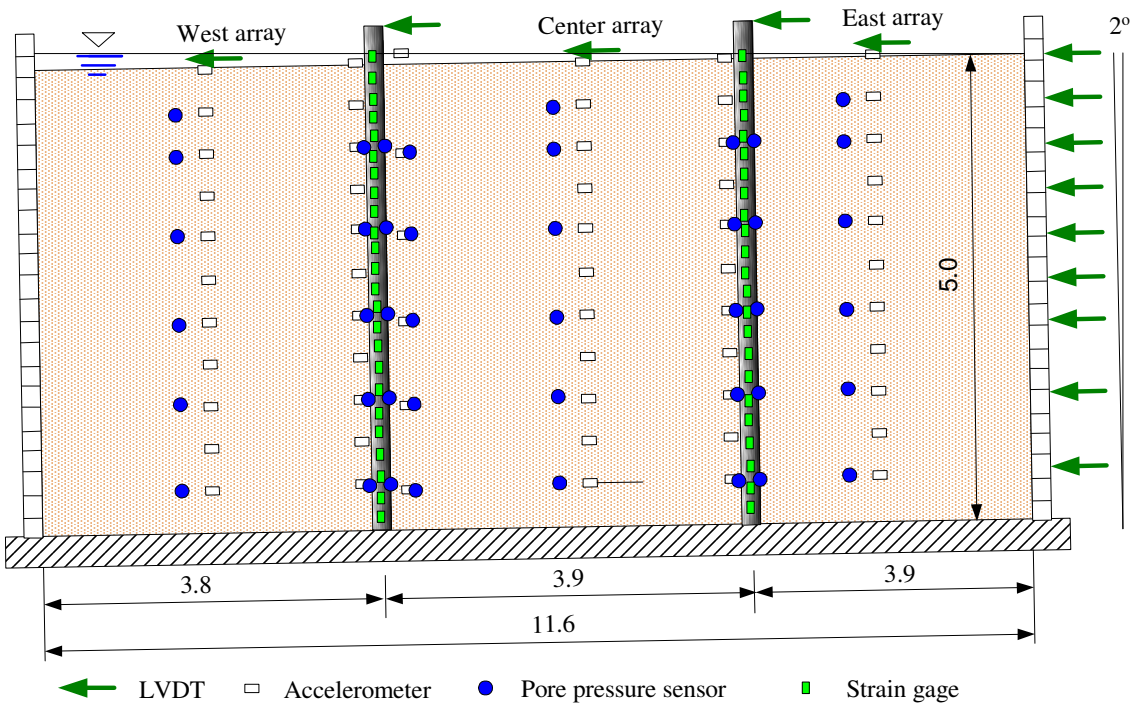

Figure 2.1. Japan4 setup and instrumentation (He 2005)

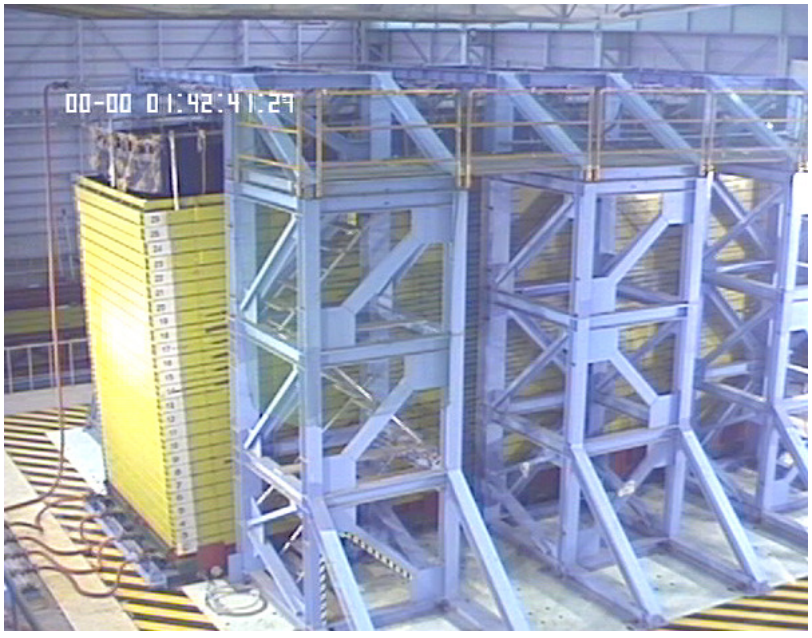

Figure 2.2. NIED, Tsukuba, Japan Laminar Soil Box, before Test (Elgamal 2008)

Figure 2.3. NIED, Tsukuba, Japan, 5m high Single Test Pile (Elgamal 2008)

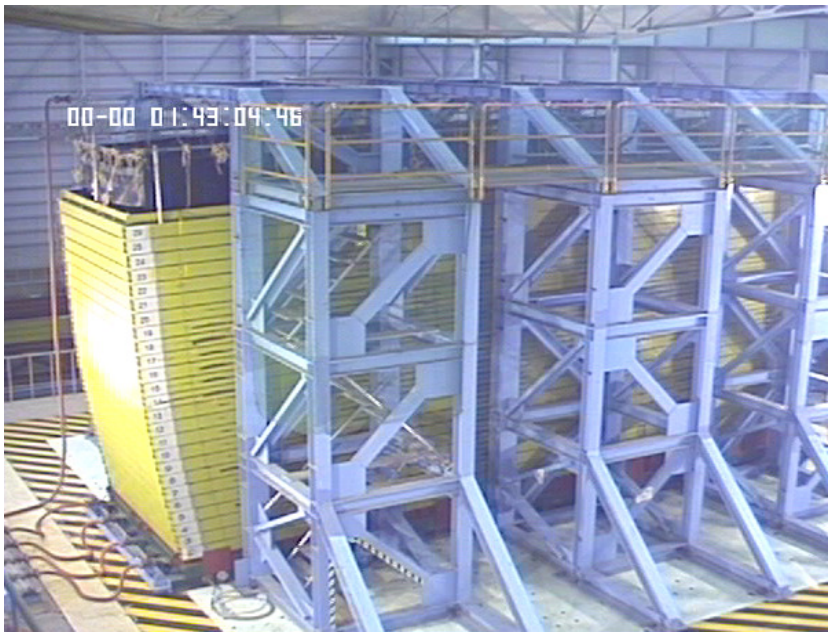

Figure 2.4. NIED, Tsukuba, Japan Laminar Soil Box, 1m of lateral spreading (Elgamal 2008)

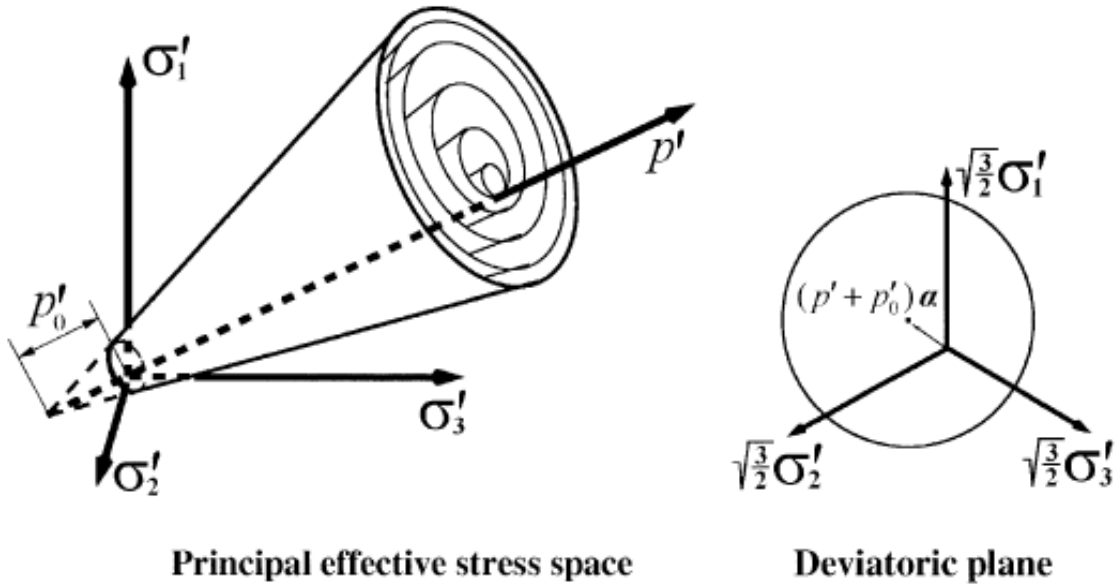

Figure 2.5. Conical yield surface in principal stress space and deviatoric plane (after Prevost 1985, Parra 1996, Yang 2000, Elgamal *et al.* 2003, Yang *et al.* 2003)

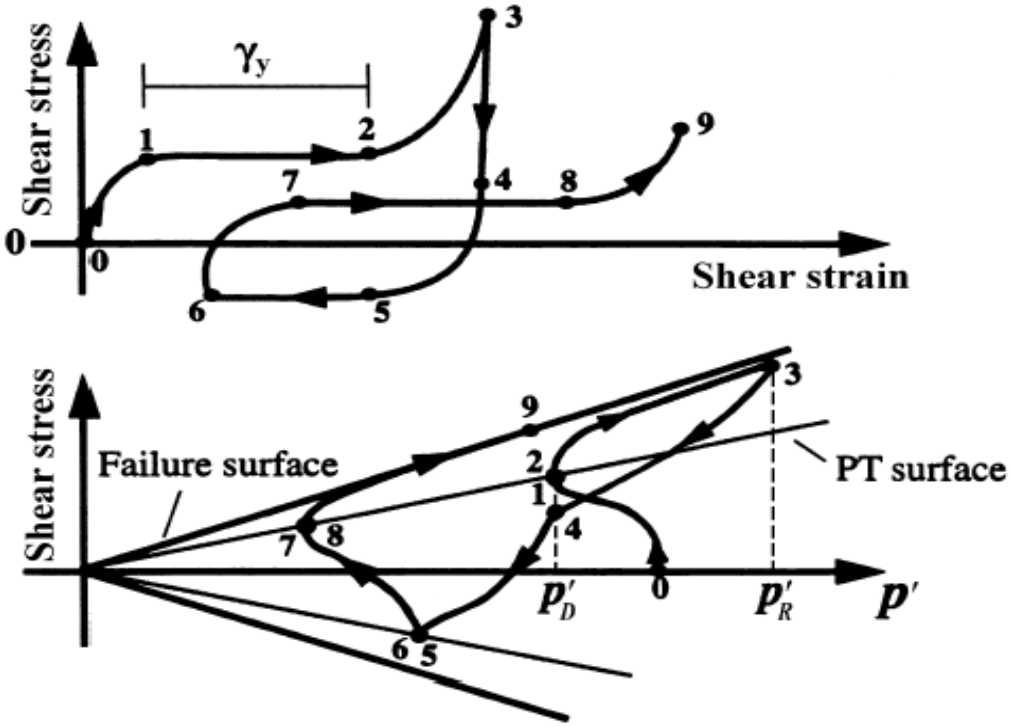

Figure 2.6. Schematic of undrained constitutive model response showing shear stress, effective confinement, and shear strain relationship (after Parra 1996, Yang 2000, Elgamal *et al.* 2003, Yang *et al.* 2003)

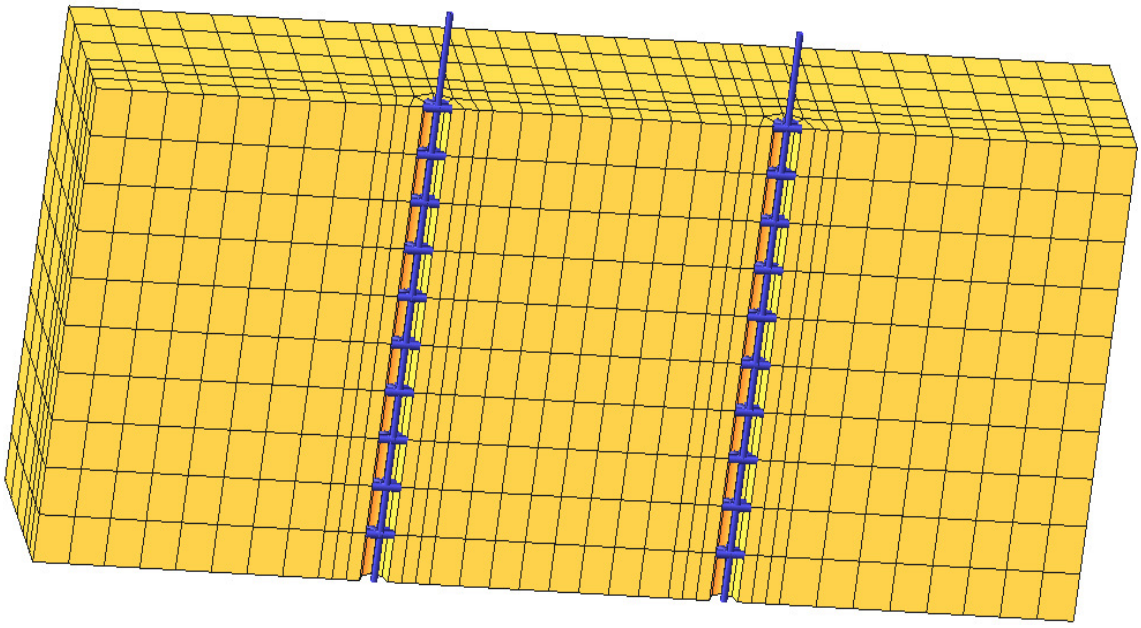

Figure 2.7. Finite element model (see He 2005 for dimensions)

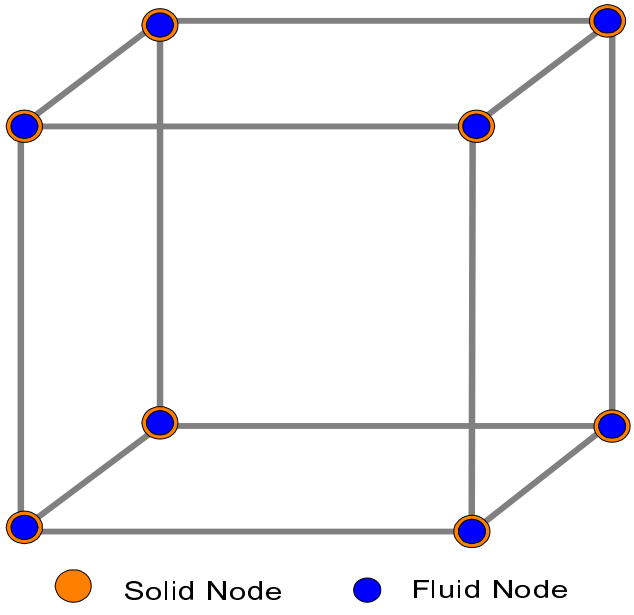

Figure 2.8. Solid-fluid fully coupled 3D 8-8 node element (He 2005)

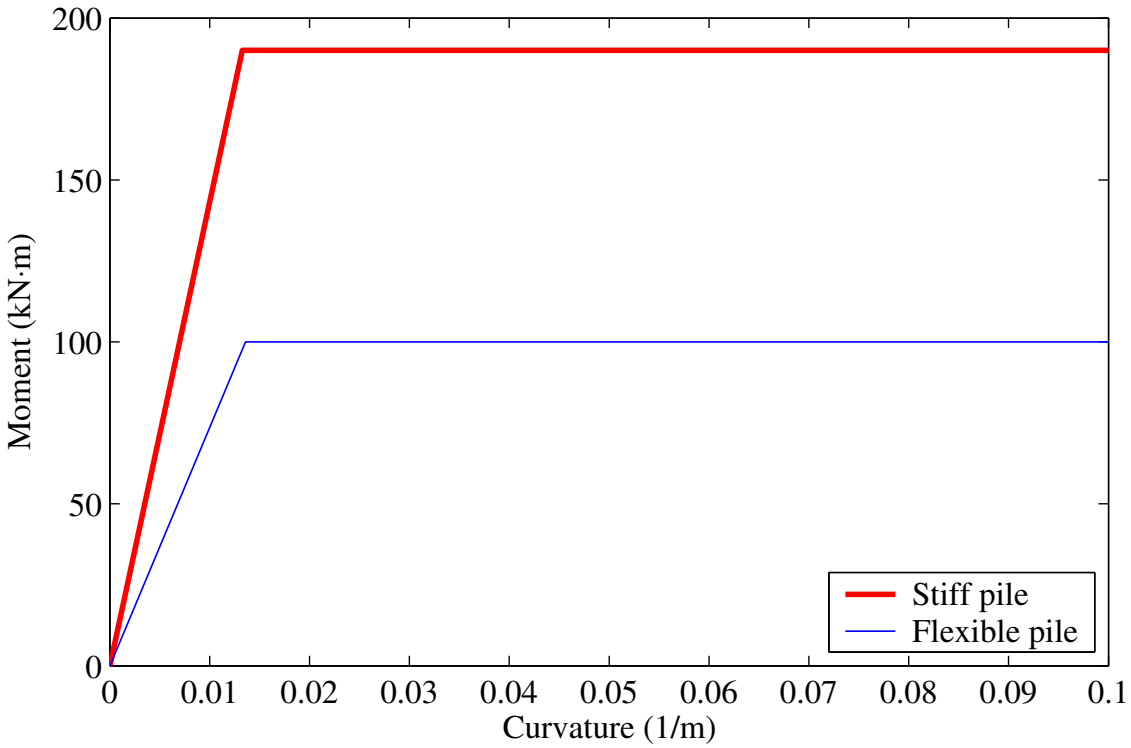

Figure 2.9. Nonlinear moment curvature relationship of the piles employed in the numerical simulation (He 2005).

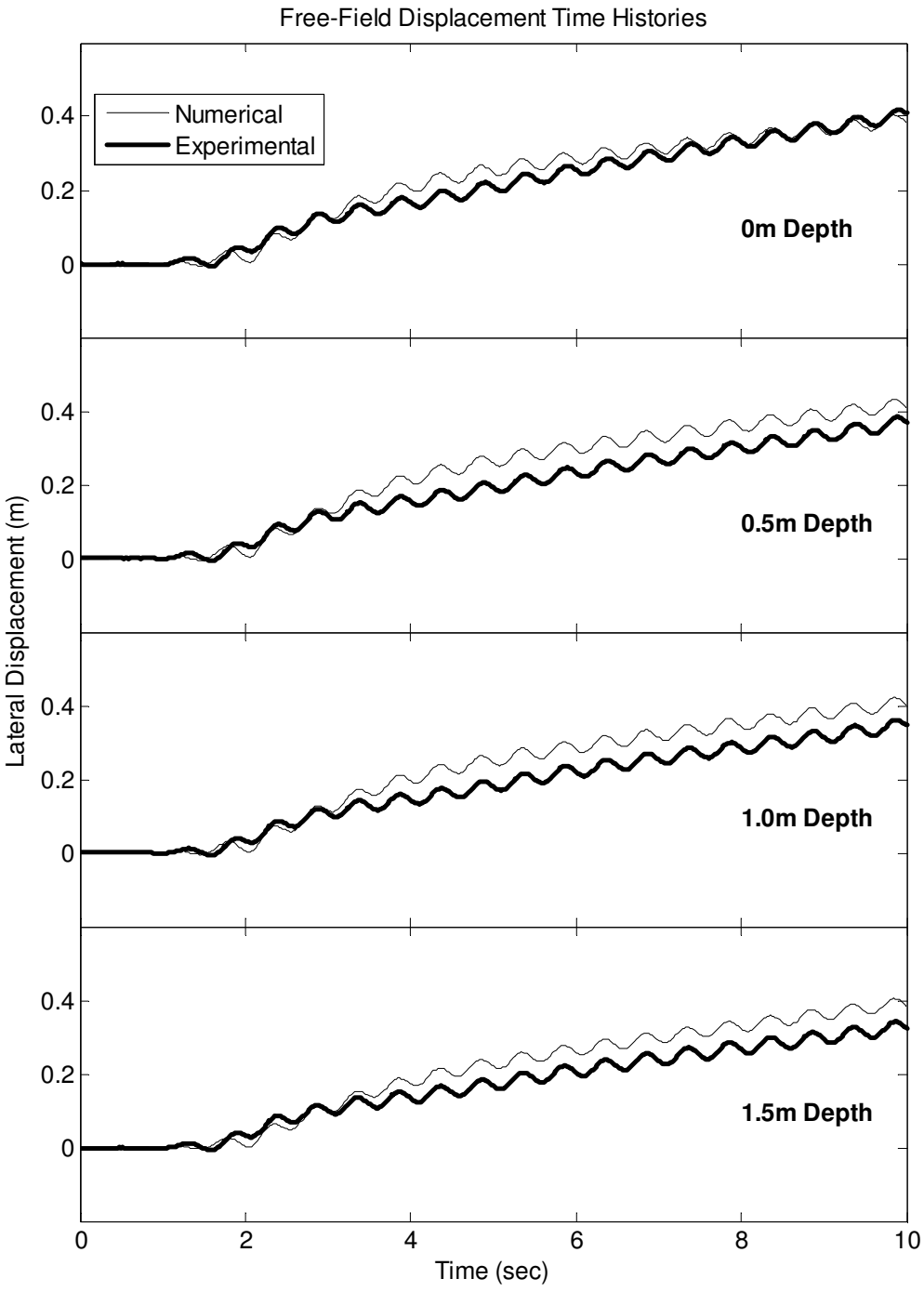

Figure 2.10. Recorded and computed free-field displacements

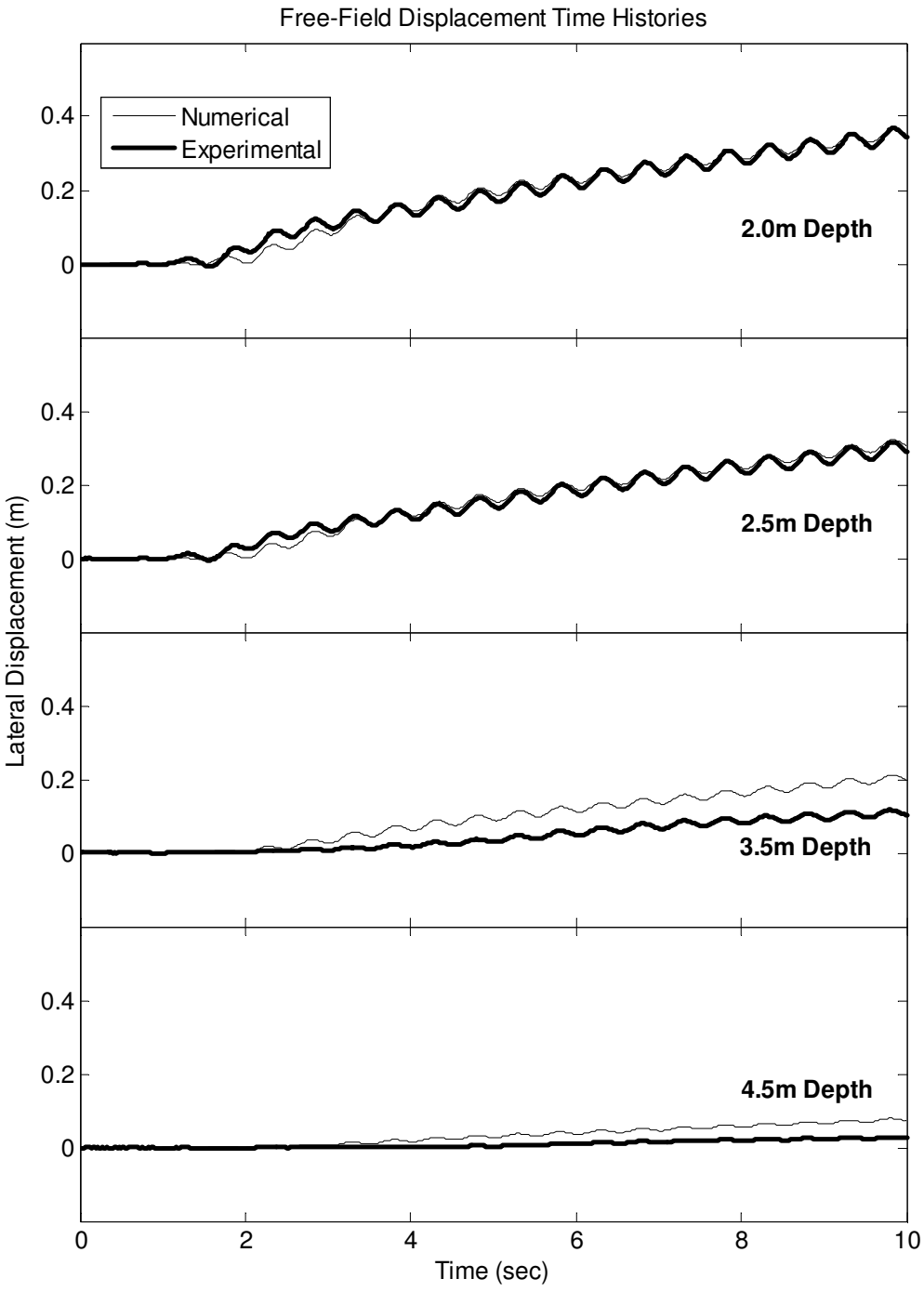

Figure 2.10. Recorded and computed free-field displacements (cont'd)

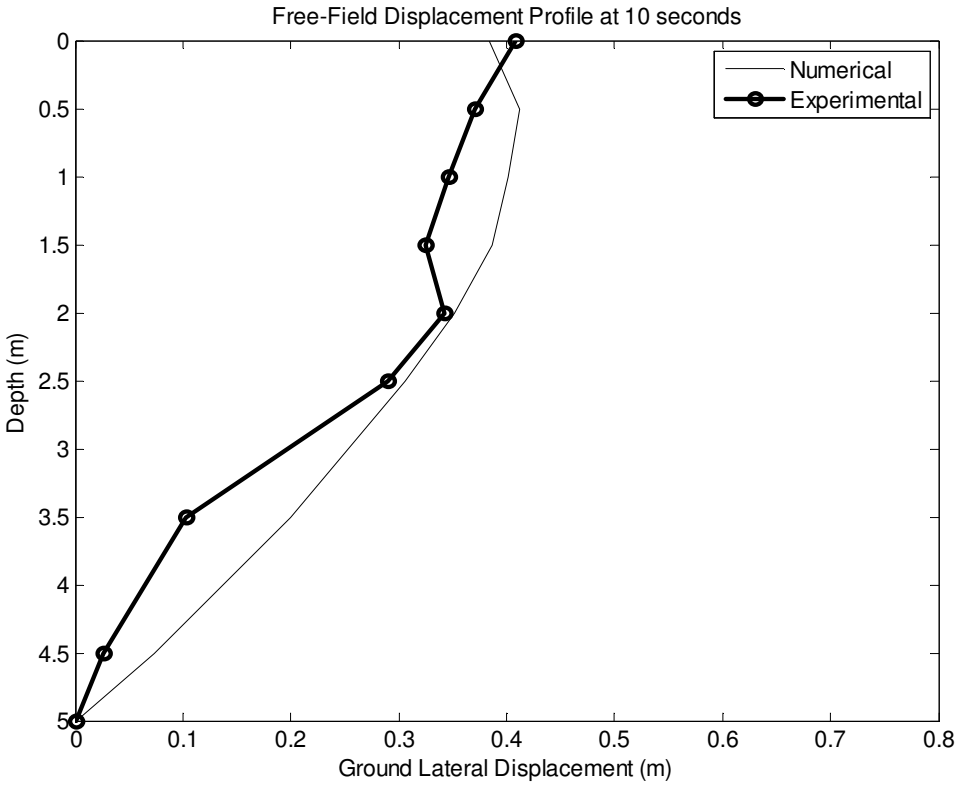

Figure 2.11. Recorded and computed free-field displacement profile at 10 seconds

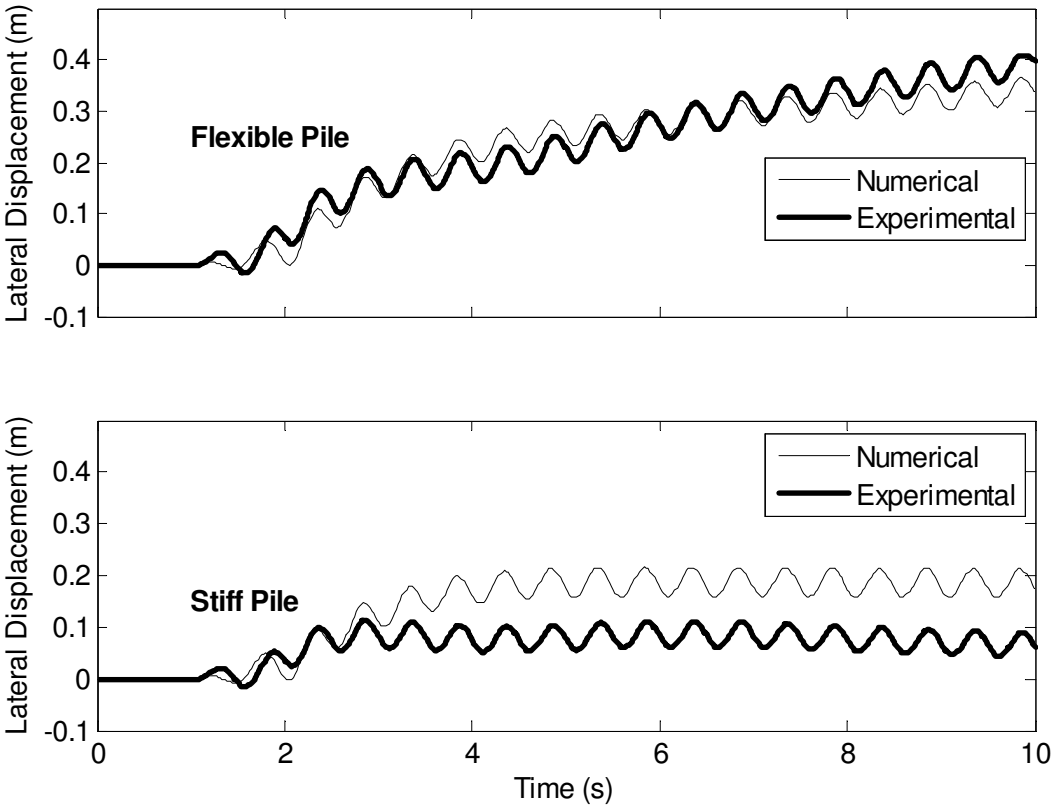

Figure 2.12. Recorded and computed pile head displacements

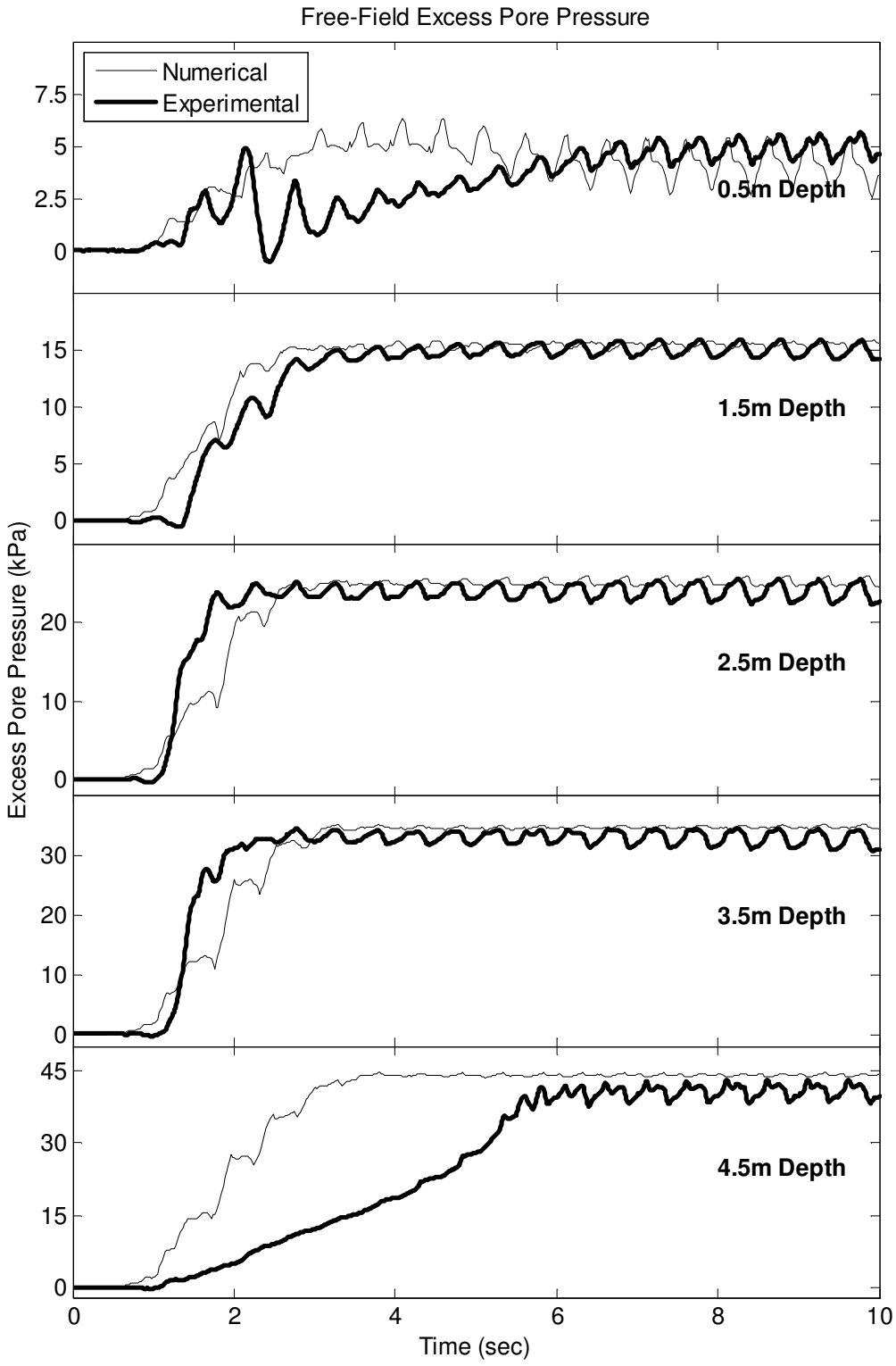

Figure 2.13. Recorded and computed free-field excess pore pressures

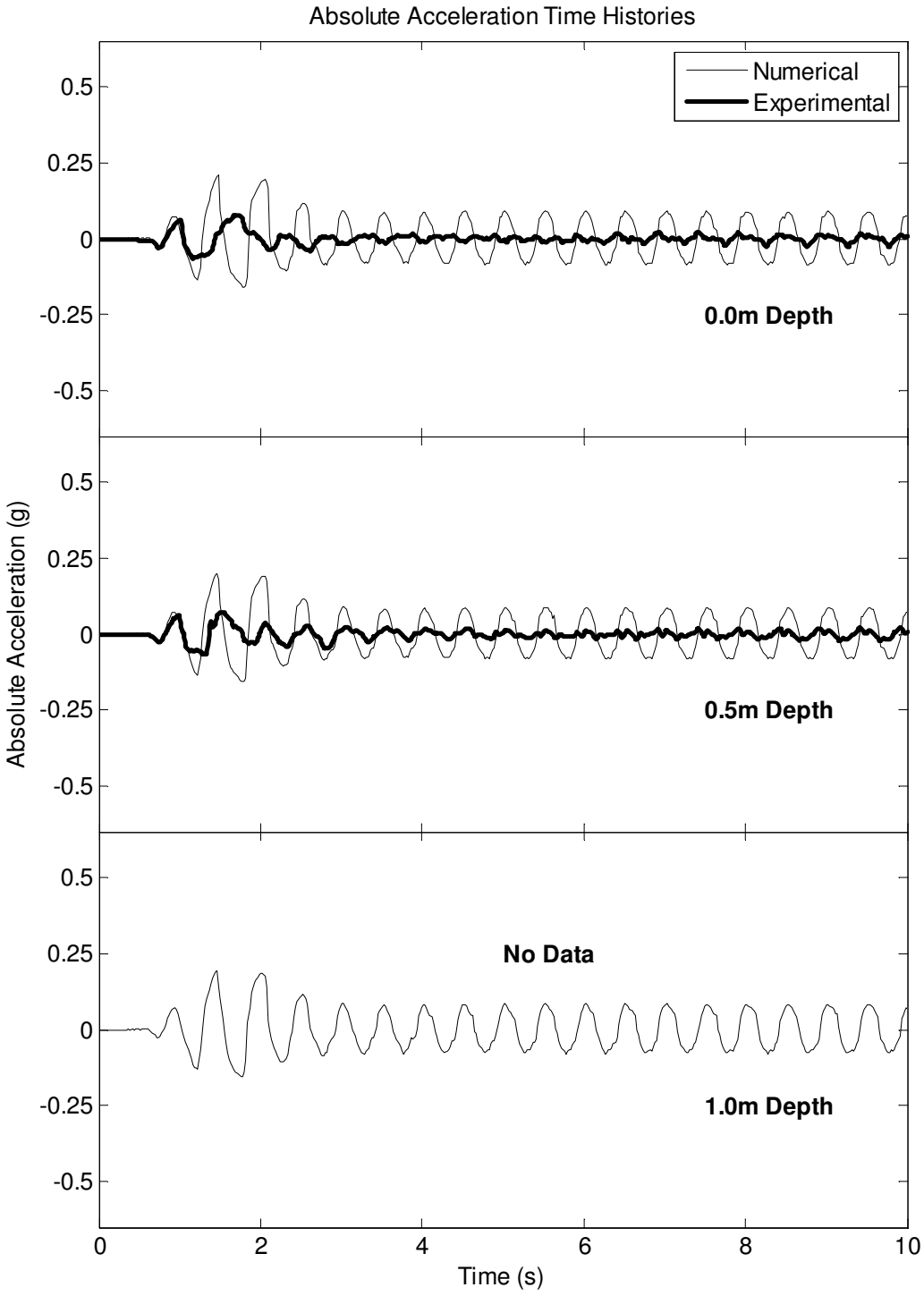

Figure 2.14. Recorded and computed free-field acceleration time histories

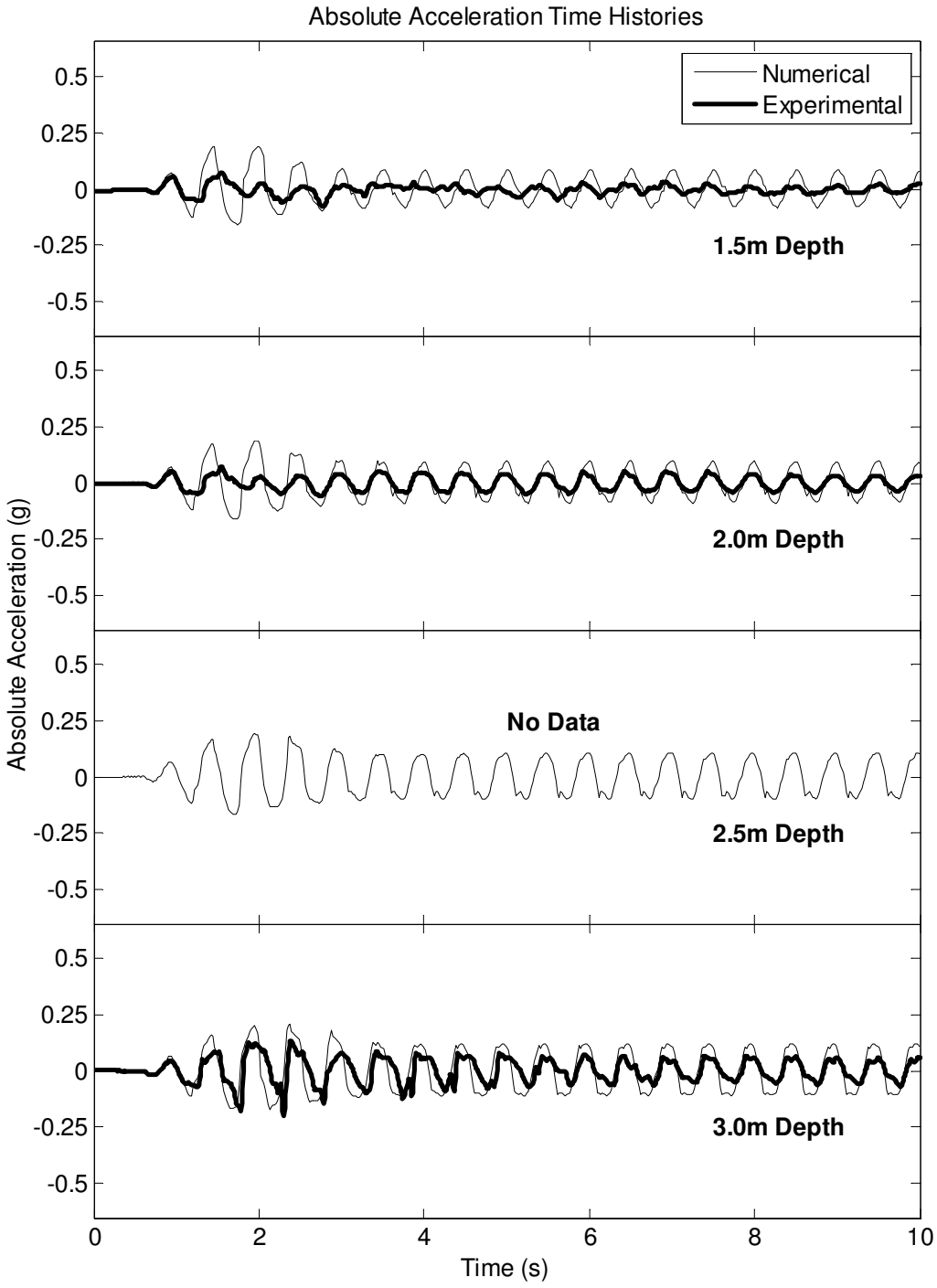

Figure 2.14. Recorded and computed free-field acceleration time histories (cont'd)

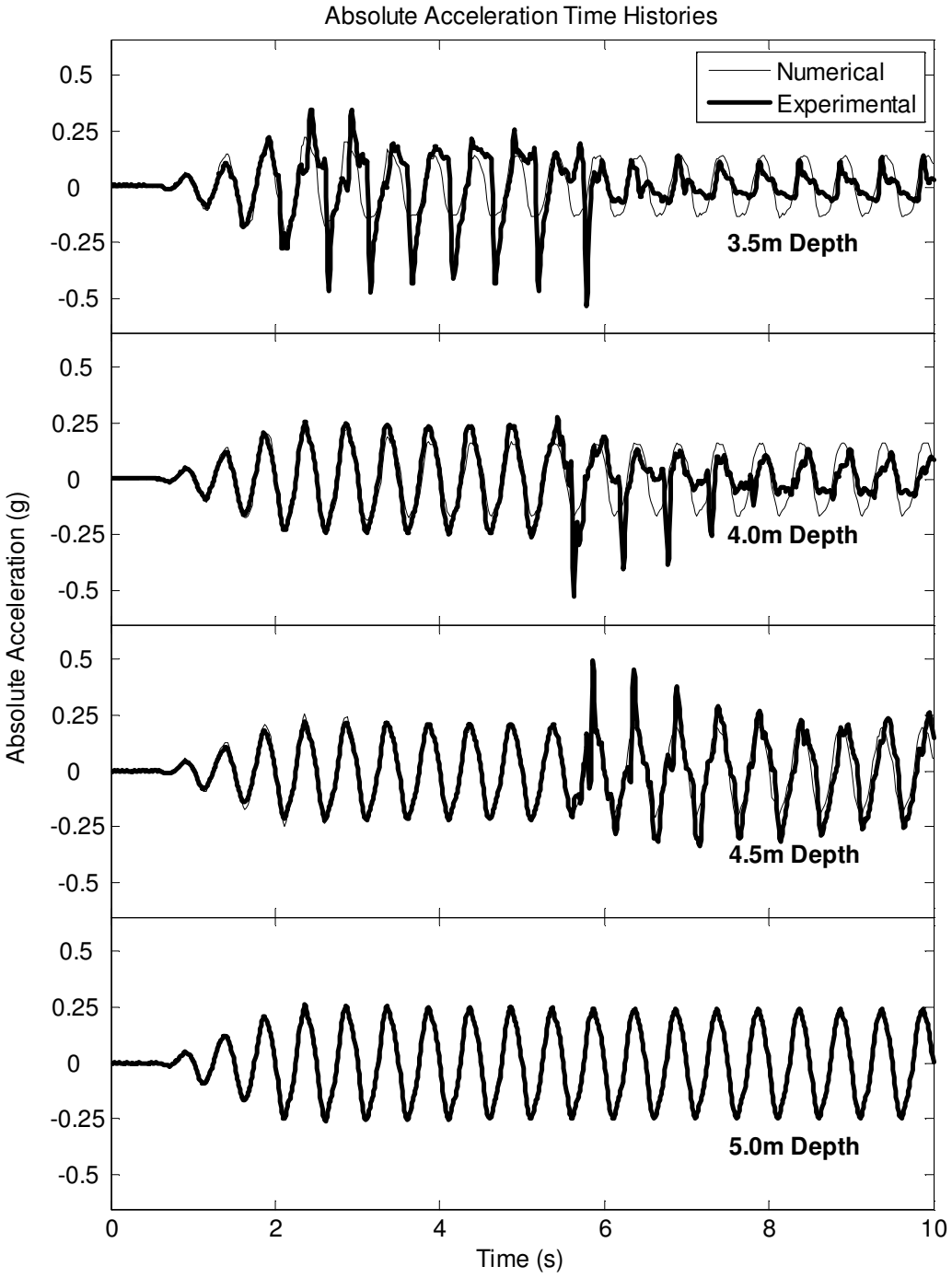

Figure 2.14. Recorded and computed free-field acceleration time histories (cont'd)

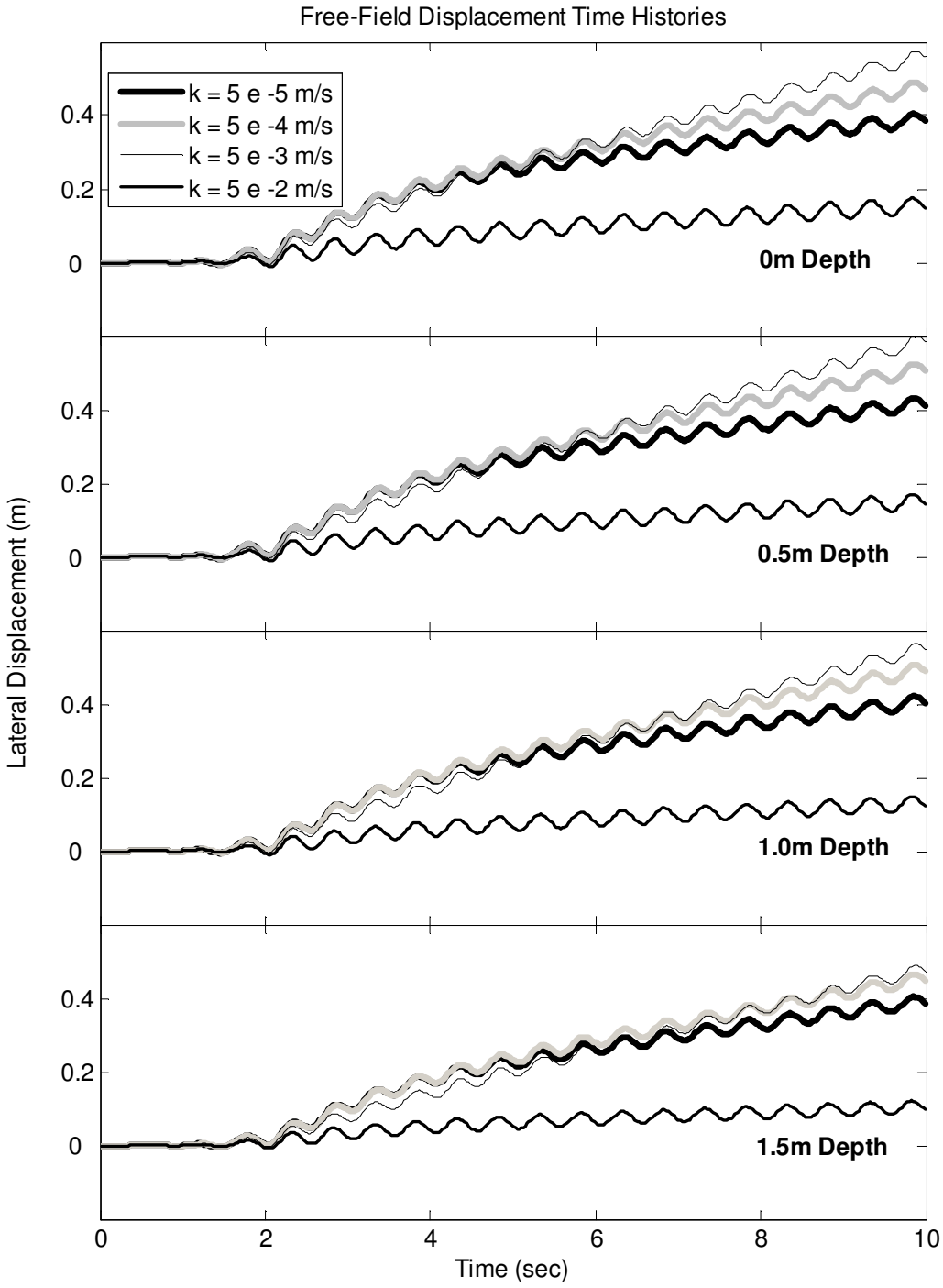

Figure 2.15. Influence of permeability on free-field displacements

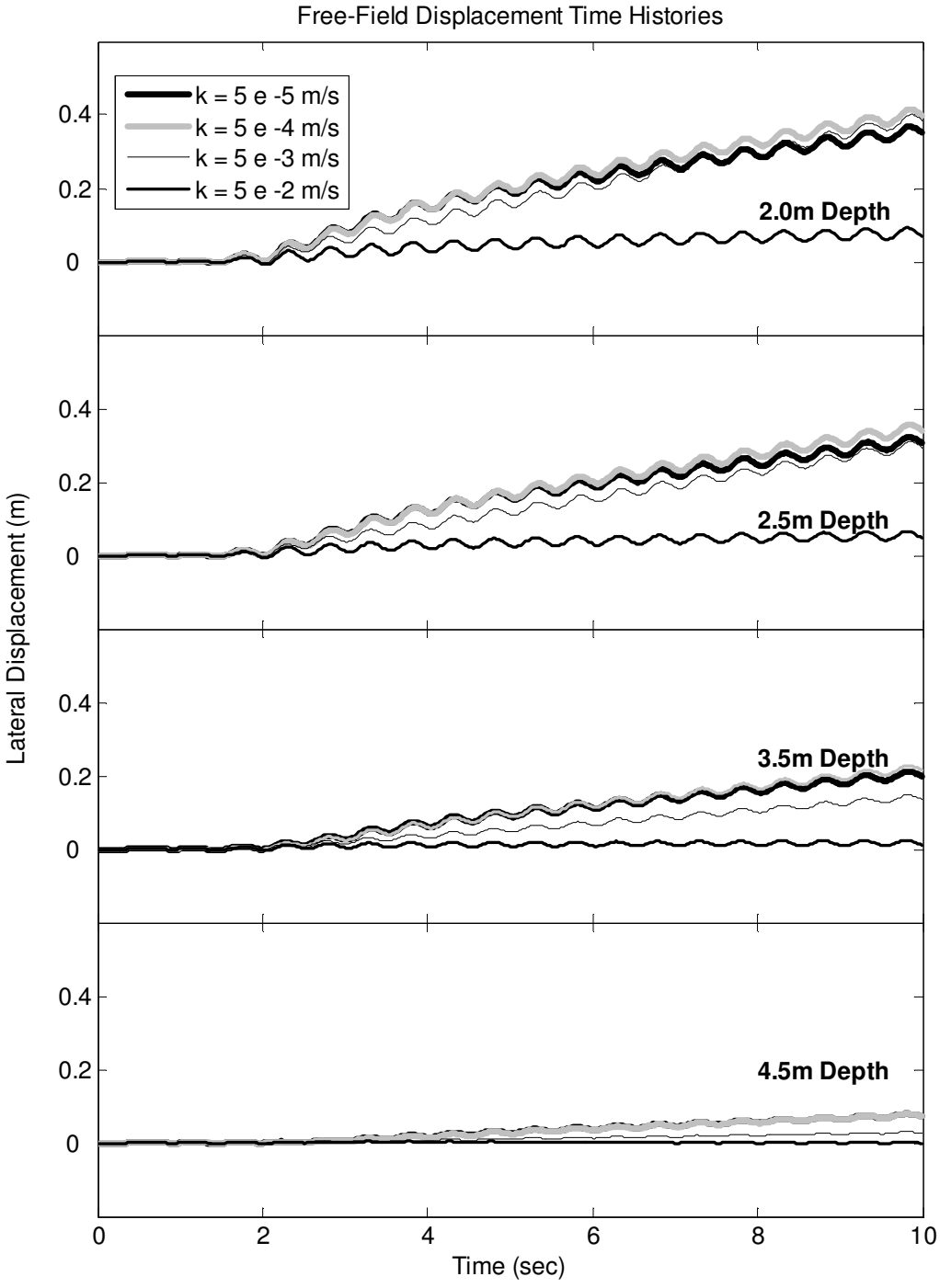

Figure 2.15. Influence of permeability on free-field displacements (cont'd)

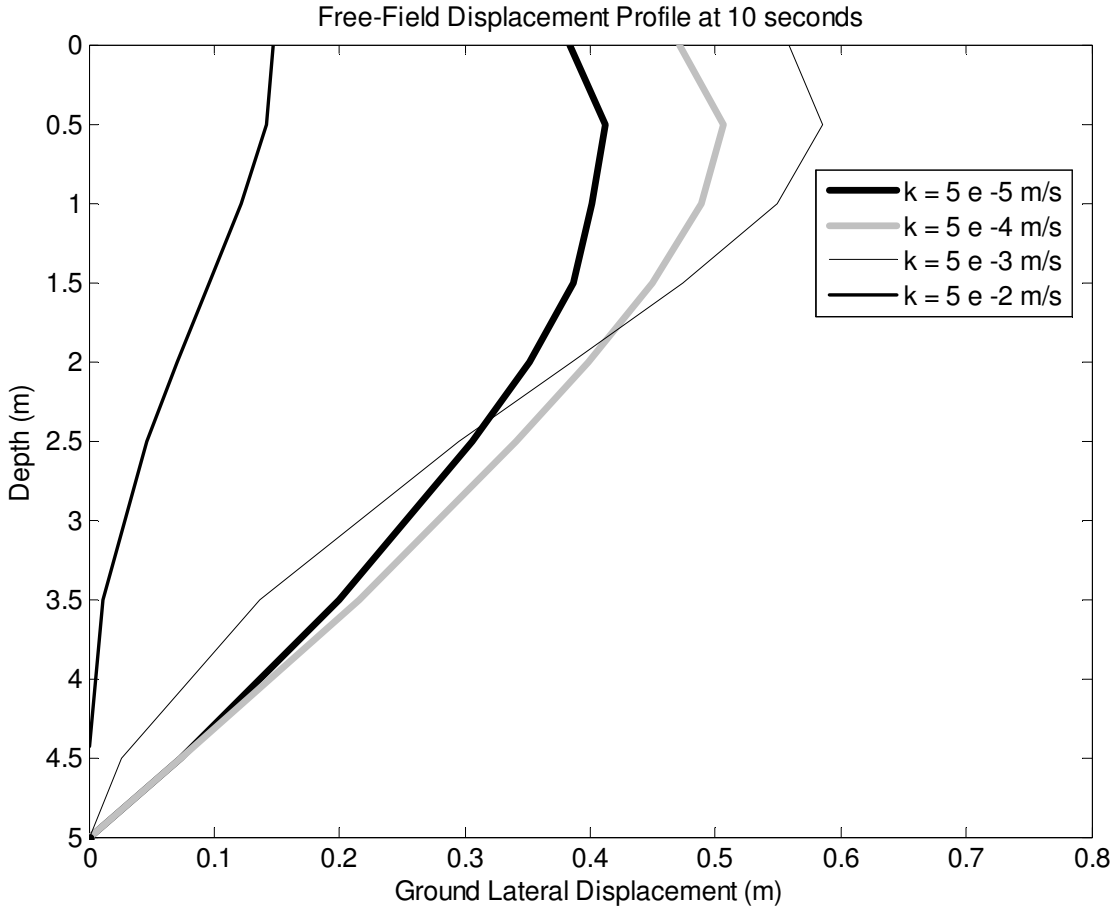

Figure 2.16. Influence of permeability on free-field displacement profile at 10 seconds, representative cases

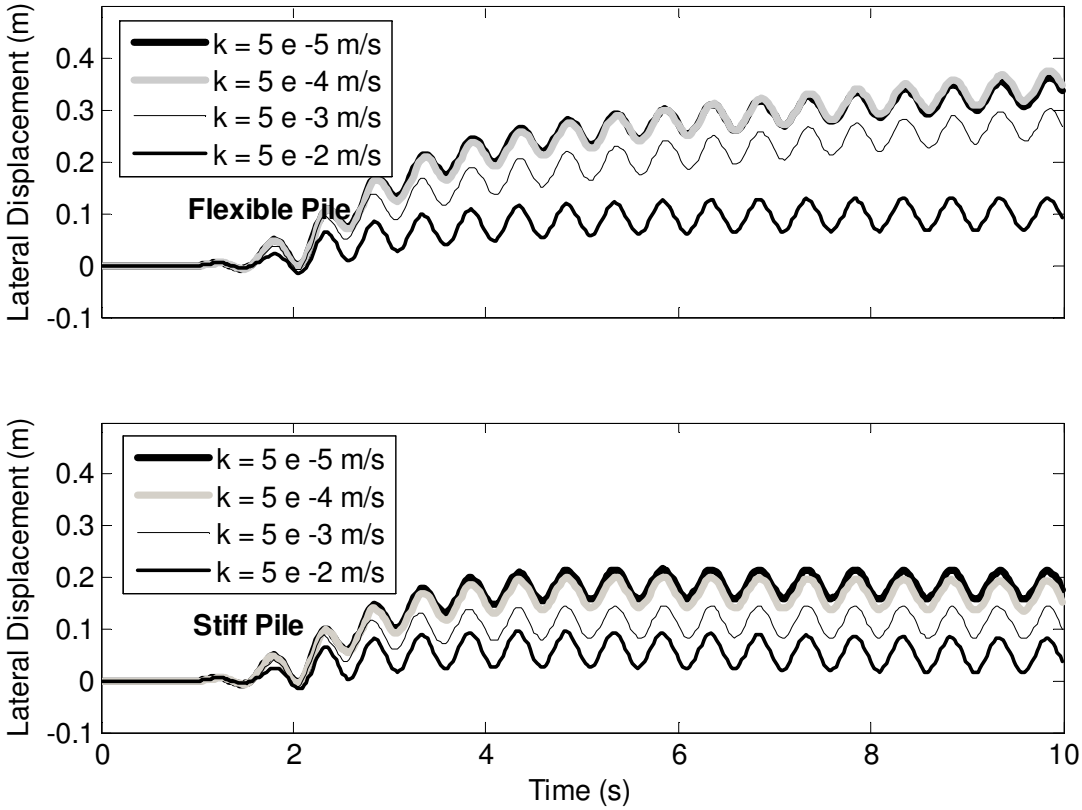

Figure 2.17. Influence of permeability on pile head displacements

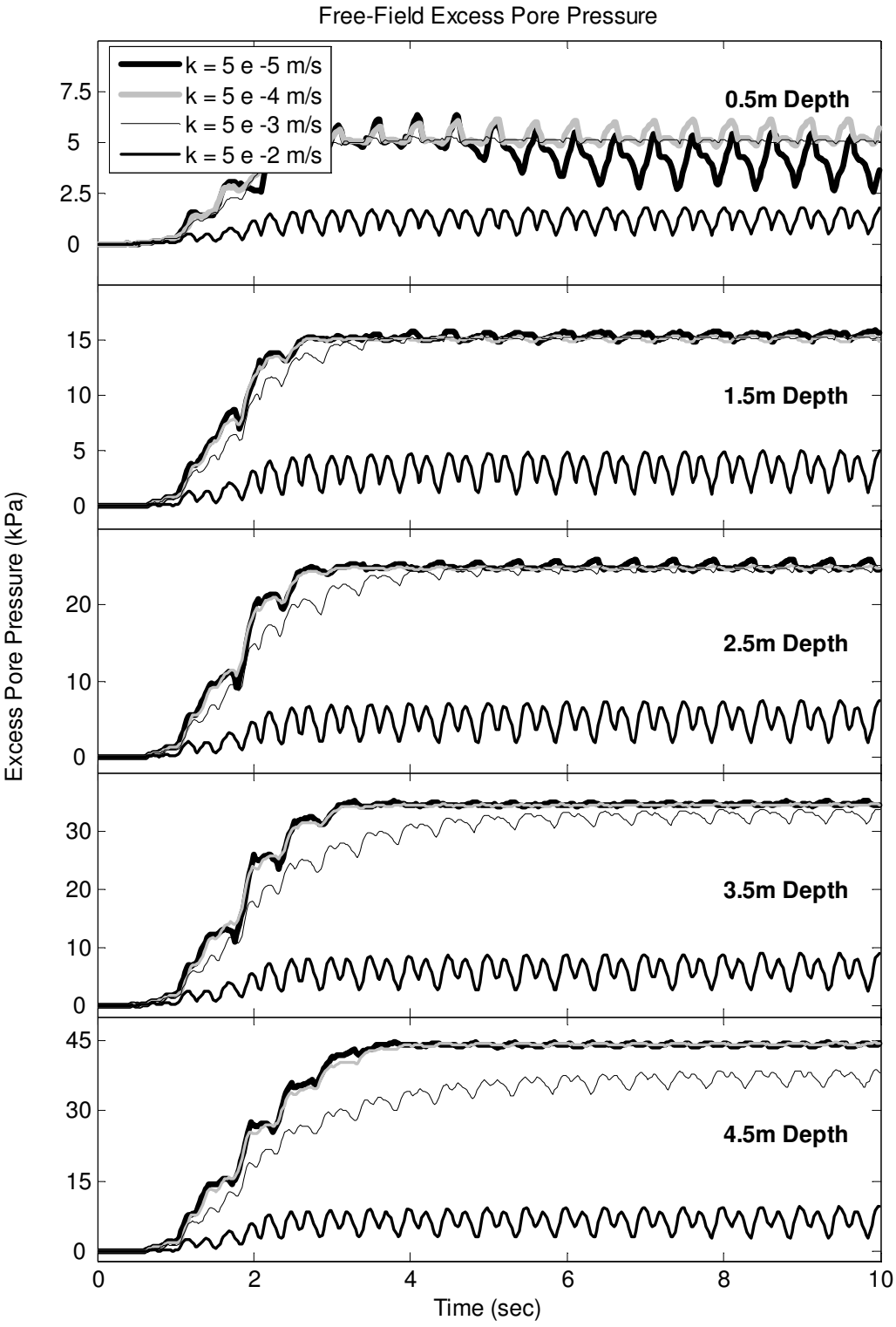

Figure 2.18. Influence of permeability on free-field excess pore pressures

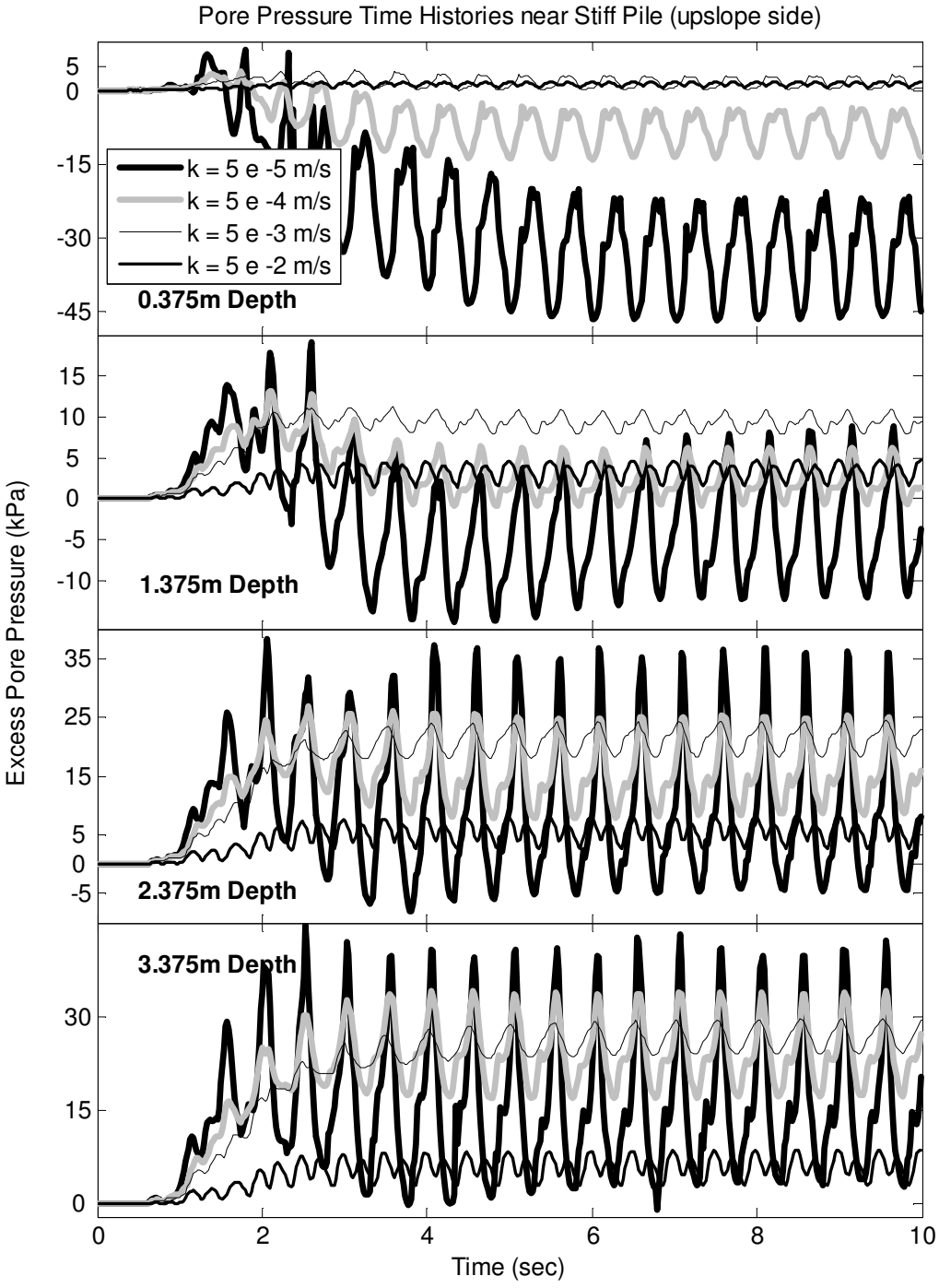

Figure 2.19. Influence of permeability on
pore pressure time histories near stiff pile (upslope side)

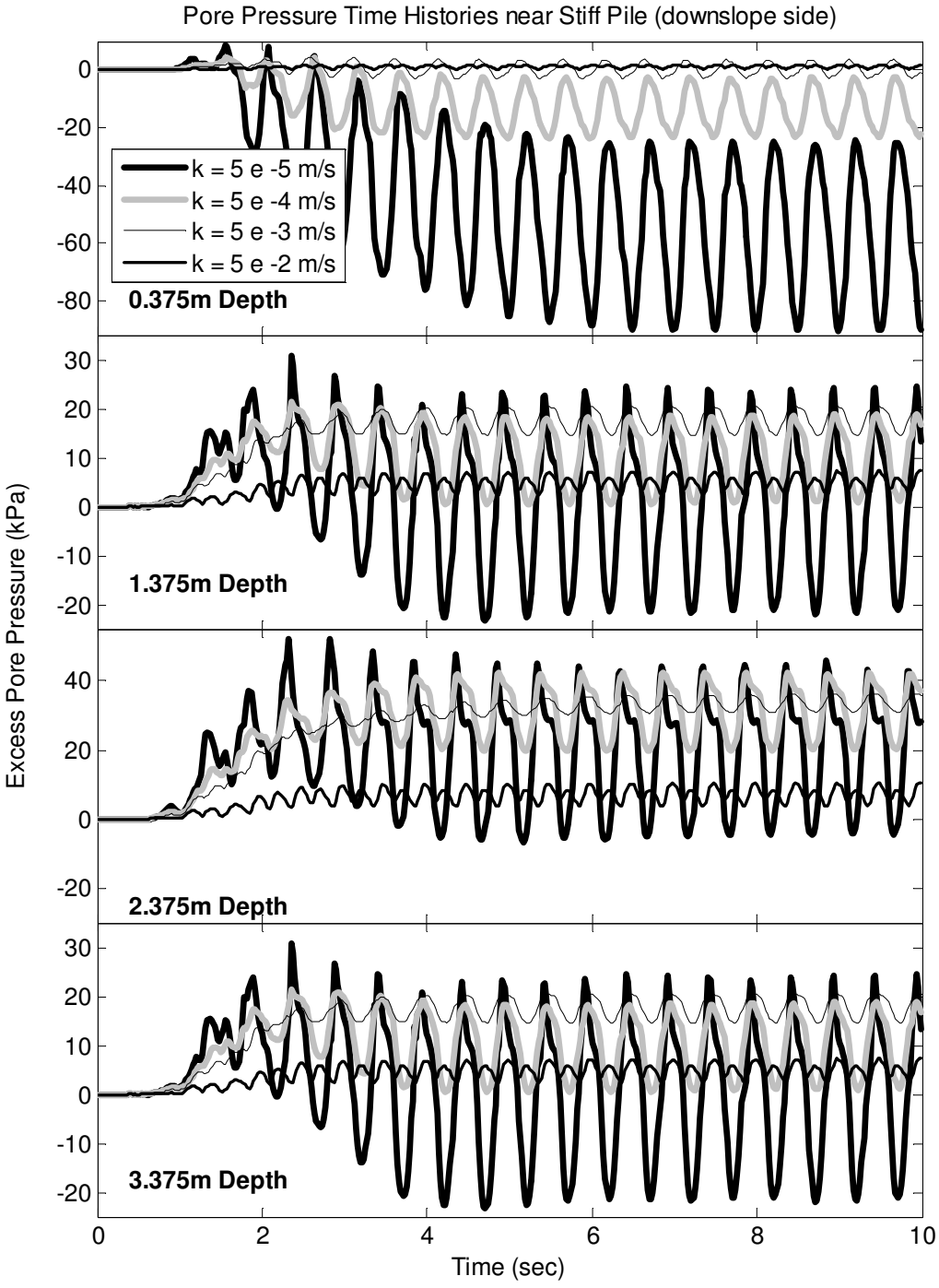

Figure 2.20. Influence of permeability on
pore pressure time histories near stiff pile (downslope side)

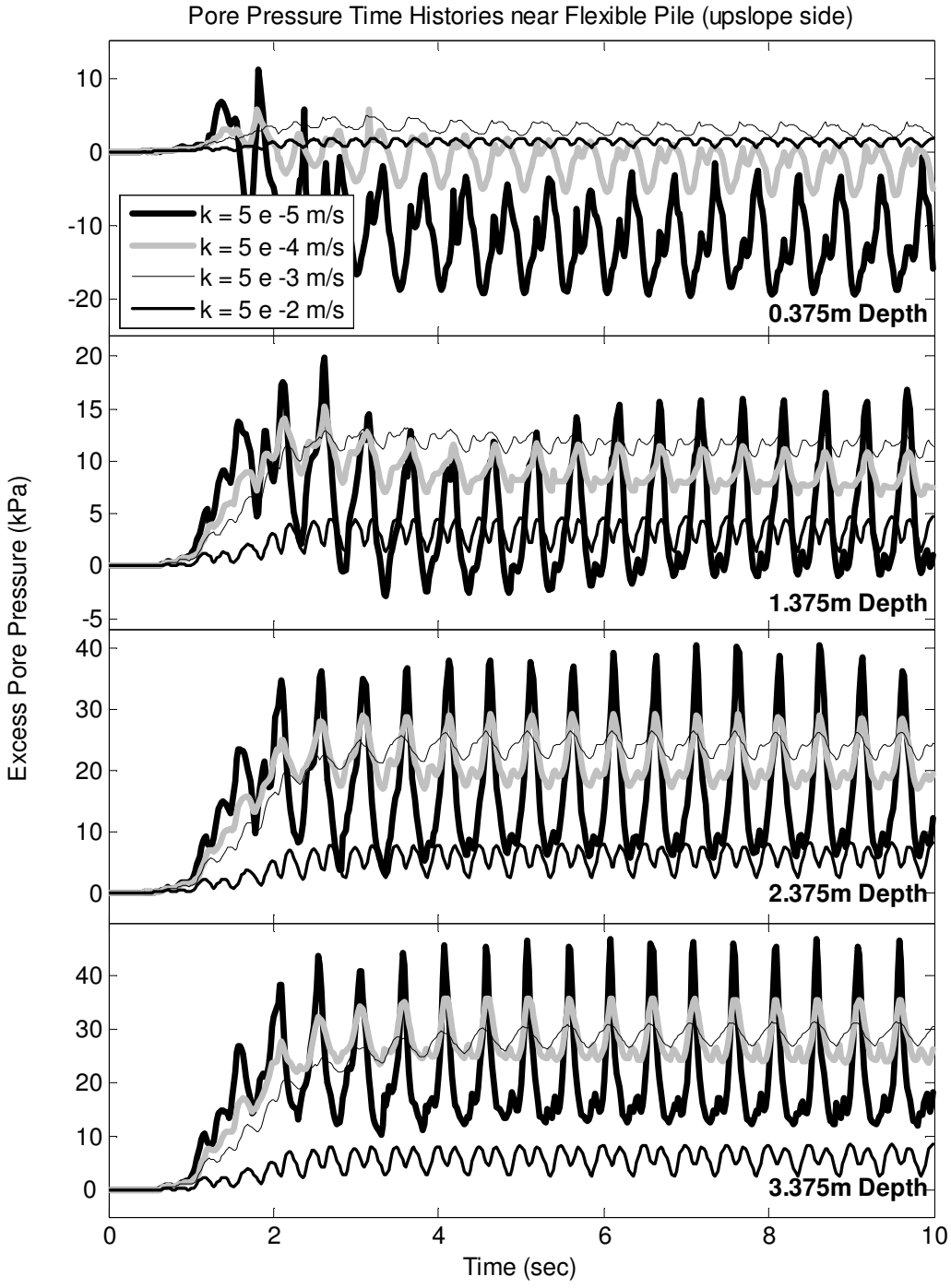

Figure 2.21. Influence of permeability on
pore pressure time histories near flexible pile (upslope side)

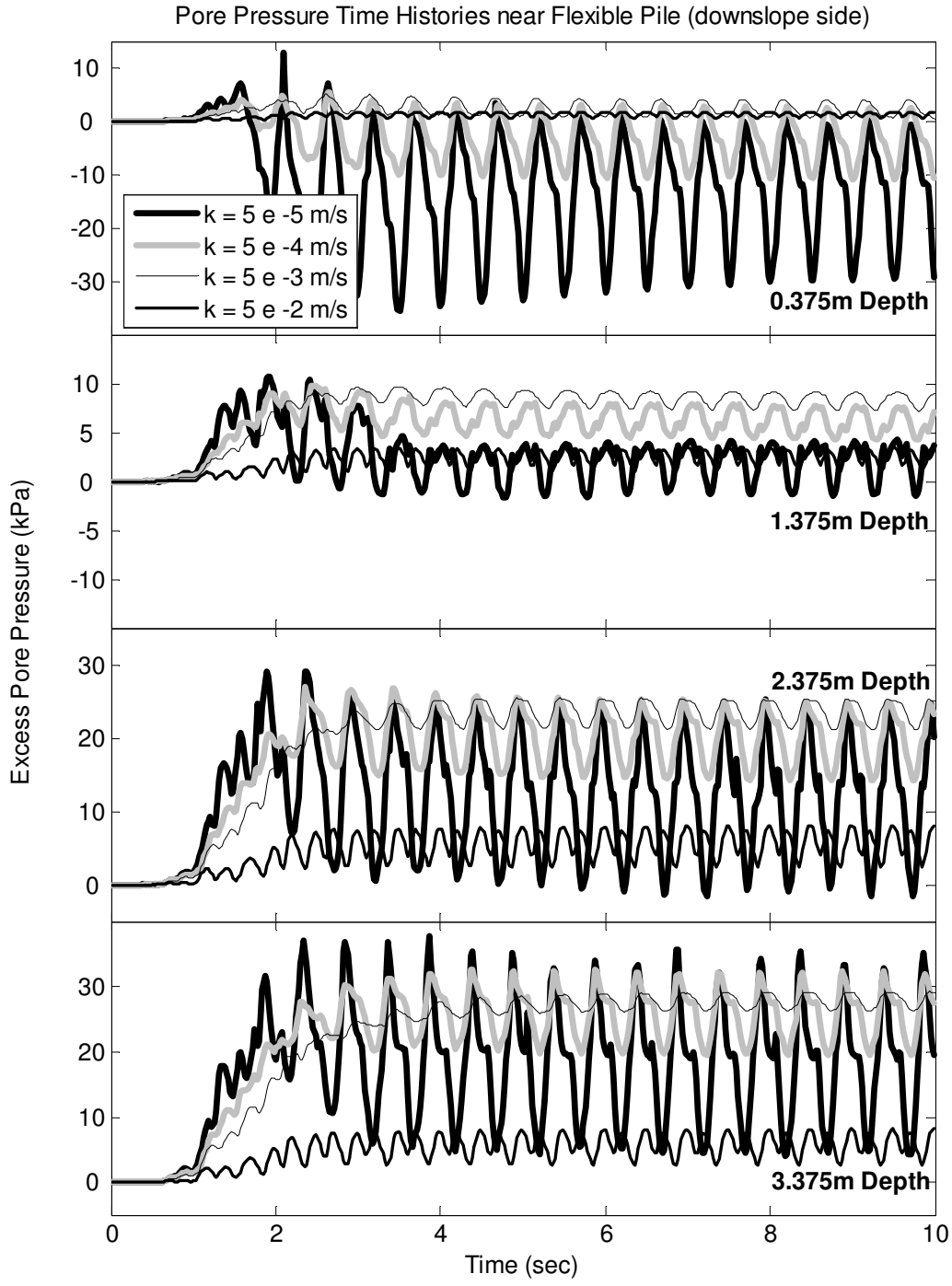

Figure 2.22. Influence of permeability on
pore pressure time histories near flexible pile (downslope side)

APPENDIX 2.1: Additional Figures for Chapter 2

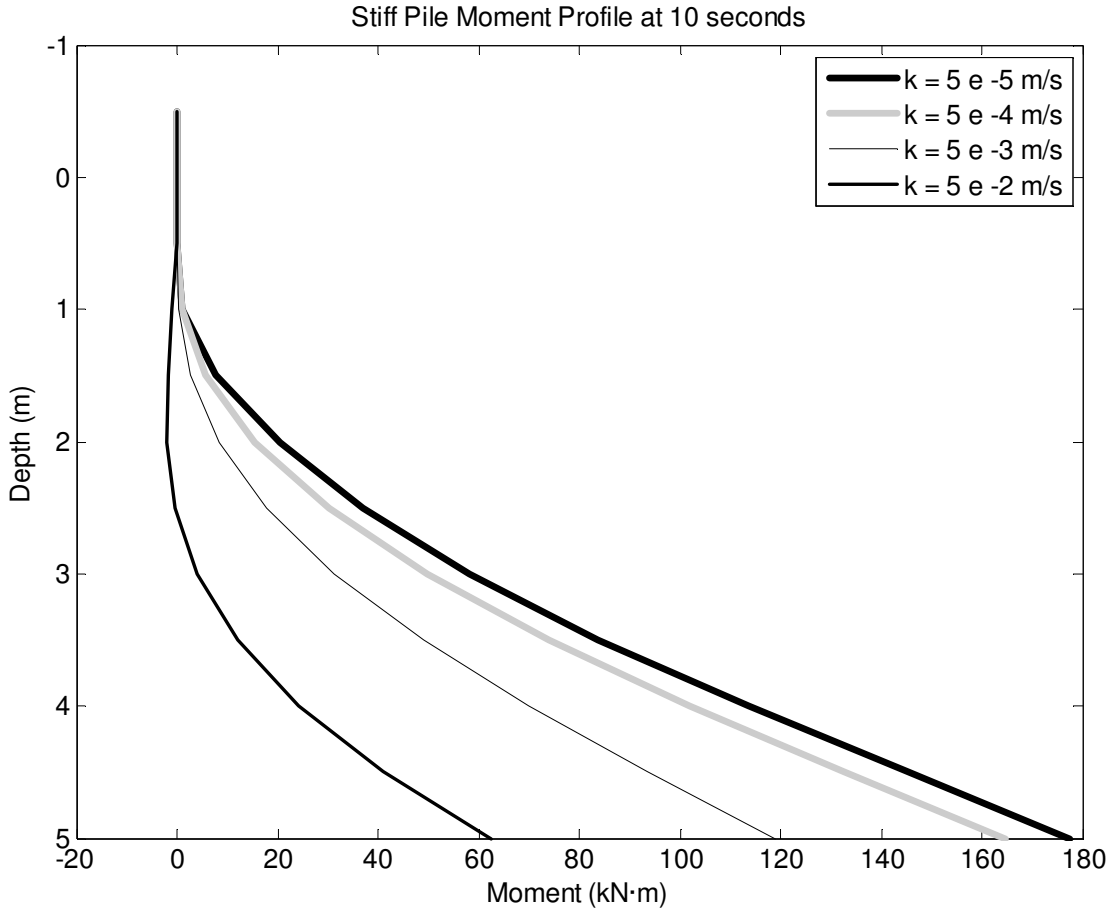

Figure 2.23. Influence of permeability on stiff pile moment profile at 10 seconds

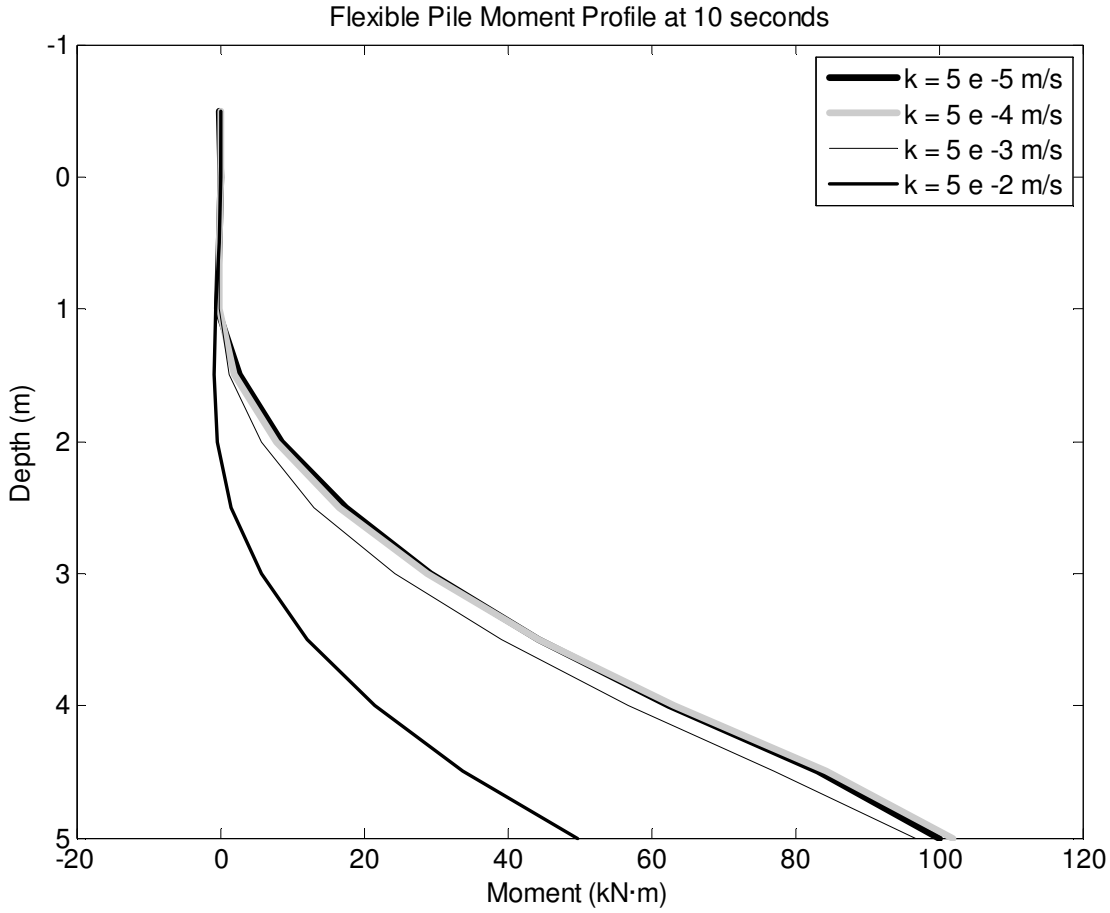

Figure 2.24. Influence of permeability on flexible pile moment profile at 10 seconds

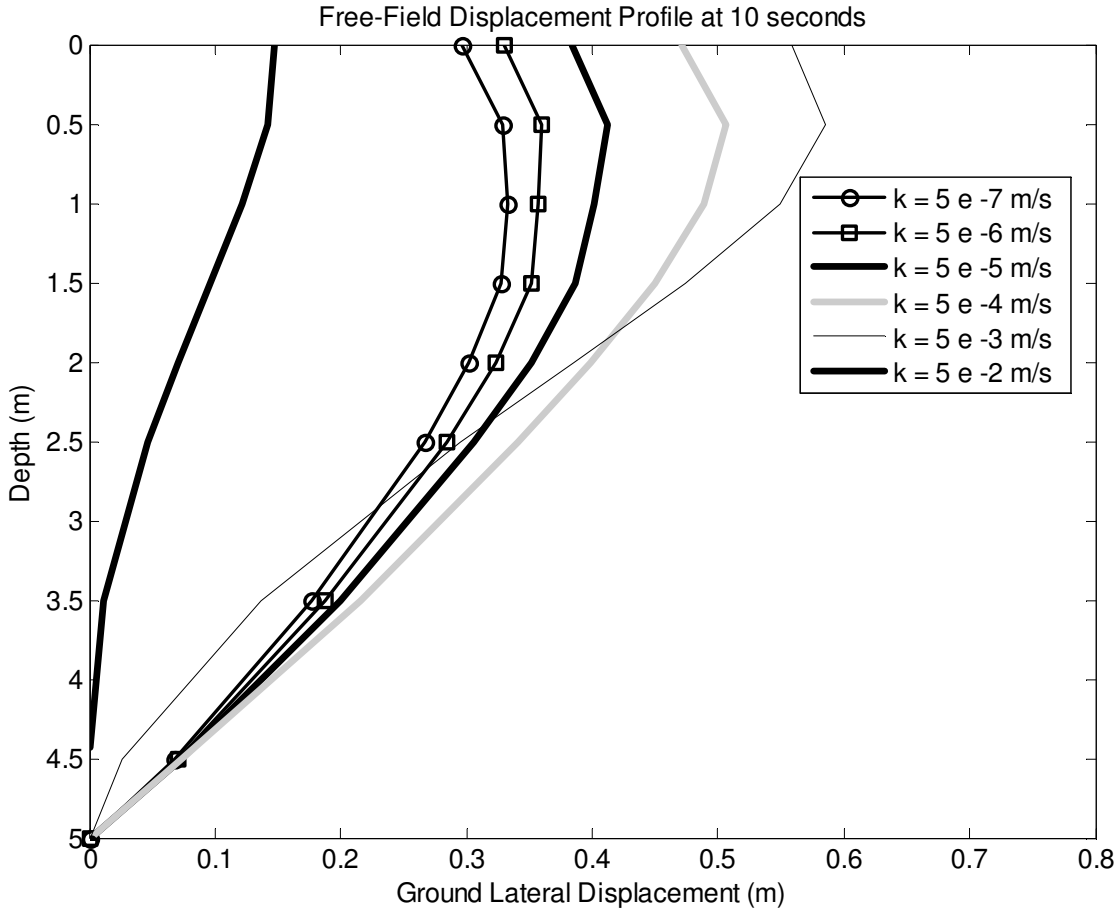

Figure 2.25. Influence of permeability on free-field displacement profile at 10 seconds (all permeability cases)

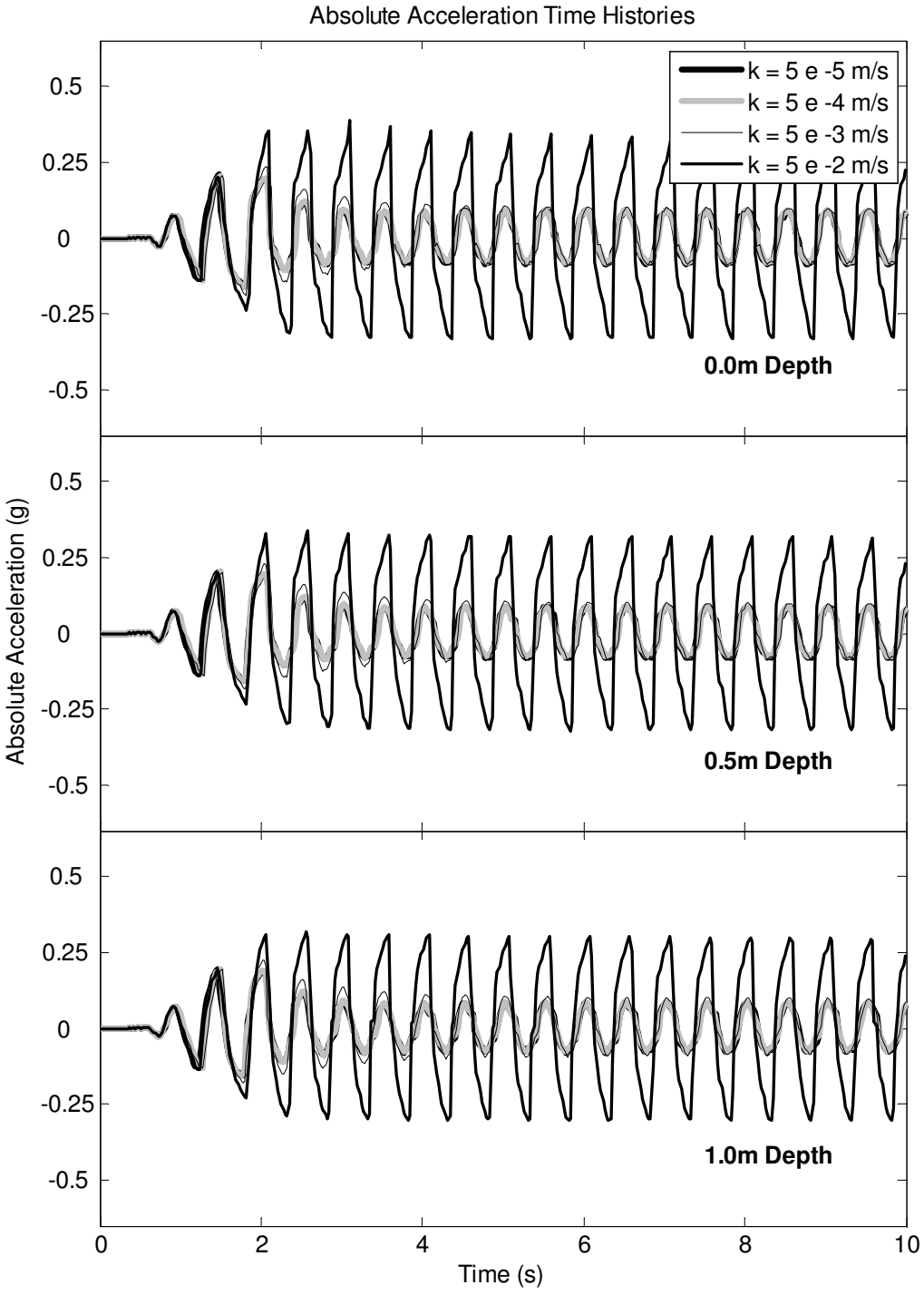

Figure 2.26. Influence of permeability on free-field acceleration time histories

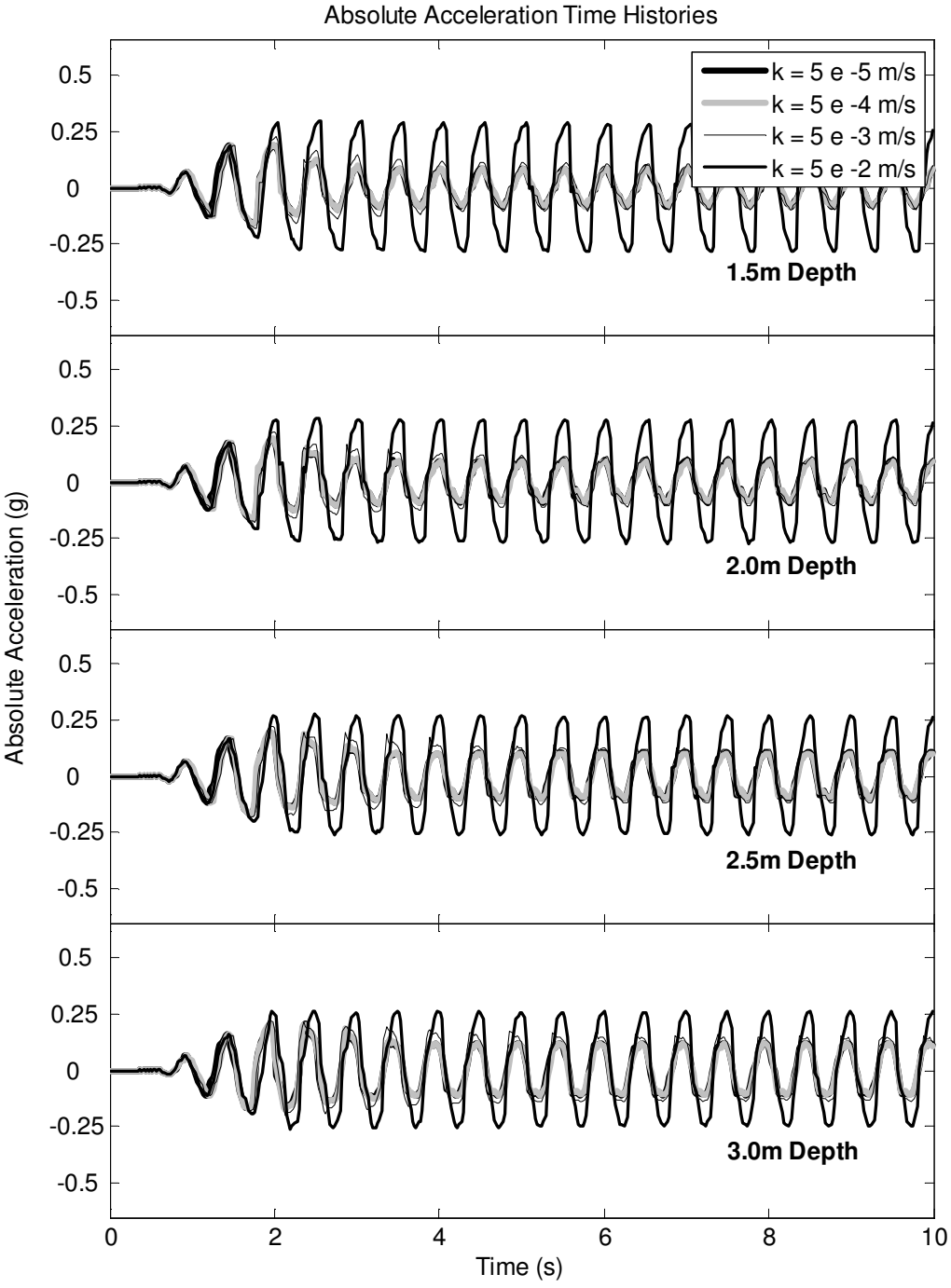

Figure 2.26. Influence of permeability on free-field acceleration time histories (cont'd)

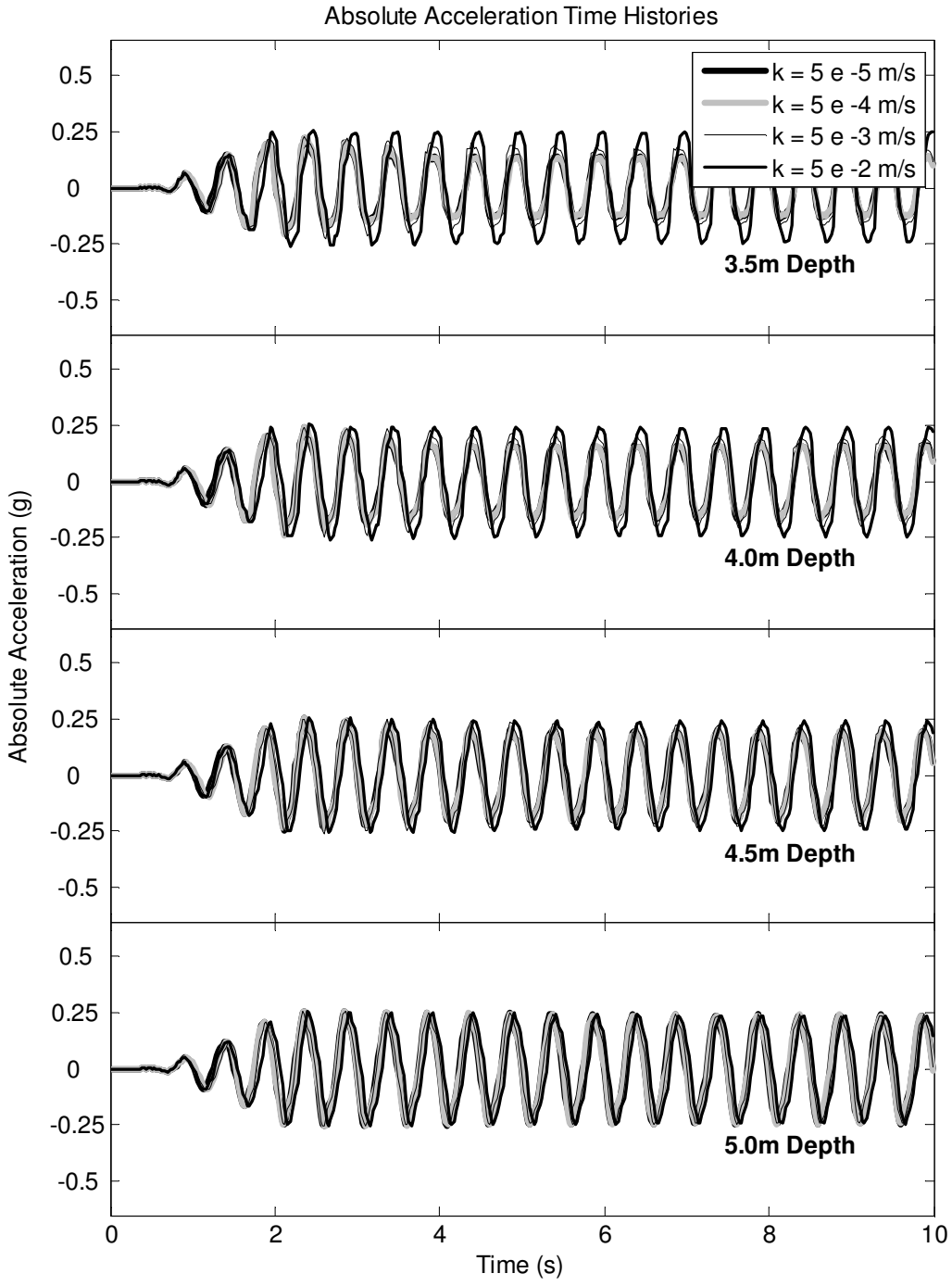

Figure 2.26. Influence of permeability on free-field acceleration time histories (cont'd)

CHAPTER 3

INVESTIGATIONS FOR VELACS SAND

3.1 Introduction

The experiment and FE analysis presented in Chapter 2 provided valuable information on the effect soil permeability has on the soil stratum and on the pile loads. This chapter presents additional investigations on the effect of soil permeability for a soil exhibiting a more noticeable tendency for dilation. First, a brief description of the representative experiment, consisting of centrifuge testing, is presented. The model parameters used to reach a calibrated FE model for this particular soil are then highlighted. Finally, results of the FE simulations are discussed, examining the pore pressure buildup, soil lateral deformation, and pile displacement.

3.2 Centrifuge Test For Calibration

3.2.1 Centrifuge Test Setup

The VELACS Model 2 simulation reported by Taboada (1995) provided valuable experimental data that was used to calibrate our model. The test was performed in a laminar box inclined at 4º to the horizontal. Nevada sand with a relative density ranging between 40-45% was deposited with water being used as the pore fluid. The experiment simulated a 10m deep soil stratum with infinite lateral extent, and permeability 50 times less than that of the prototype soil used.

Linear Variable Differential Transducers (LVDTs) were mounted on the laminar box exterior to measure free-field lateral displacement. The model was also

instrumented with accelerometers and pore pressure transducers within the soil stratum. The above-described setup can be observed in Figure 3.1.

3.2.2 VELACS Sand Calibration

As can be observed by Figure 3.1, the data obtained from VELACS Model 2 came from sensors located at different depths in comparison with the data obtained from Japan4. The output generated by the FE model was given at depths based on the sensor locations of Japan4 (Figure 2.1) and the calibrated FE model could not be used to compare the response output with the data obtained from VELACS Model 2. Instead, a 10 m shear column was used for calibration. The 10 m shear column employed the same FE analysis framework and soil constitutive model as the calibrated FE model for Japan4, only it allowed data to be output at the desired locations that would make it comparable to the data obtained from VELACS Model 2.

Once a satisfactory calibration was reached with the shear column model, the parameter values used were employed in the 3D finite element model making it our benchmark case for this Nevada sand with higher dilative properties. These parameters are summarized in Table 3.1 and were used in subsequent runs in which only the soil permeability was changed similarly to the investigation described in Chapter 2.

Table 3.1. Velacs sand parameters employed in the 3D analysis
(PressureDependMultiYield model in OpenSees)

	Parameter	Value
Soil Constitutive Model Parameters	Saturated mass density (g/cm^3)	1.97
	Poisson's ratio ν	0.4
	Reference Shear Modulus (kPa)	33278
	Reference Bulk Modulus (kPa)	155300
	Reference Bulk Modulus for Dynamics (kPa)	22185
	Friction angle ϕ (º)	32
	Peak Shear Strain	0.1
	Reference Pressure (kPa)	80
	Pressure Dependence Coefficient	0.5
	Phase Transformation angle ϕ_T (º)	27
	Contraction 1	0.2
	Dilation 1	0.2
	Dilation 2	2.0
	Liquefaction1	0
	Liquefaction2	0
	Liquefaction3	0
	Permeability (m/s)	$6.6x10^{-5}$
	Numerical Constant for Cohesion (kPa)	2.745
Dynamic FE Analysis Parameters	Gamma (Newmark integration parameter)	0.6
	Beta (Newmark integration parameter)	0.325
	Mass Proportional Damping	0
	Initial Stiffness Proportional Damping	0.003
	Density Multiplier	1.14
	Inclination (degrees)	3
	Fluid-solid combined bulk modulus (kPa)	2200000

3.3 FE Analysis Results

Once a reasonable match was produced for VELACS sand focusing only on overall container displacement and free-field excess pore pressure, the effects of changing soil permeability were then explored. Figure 3.2 shows a comparison in lateral displacement at different depths between the experimental data and the benchmark case, while Figure 3.3 shows a comparison between the experimental and benchmark excess pore pressures. Figure 3.4 shows the acceleration time histories for the experimental data in comparison to the benchmark case as well.

Following the satisfactory calibration depicted in Figures 3.2, 3.3 and 3.4 for VELACS sand, the influence of permeability was explored. Various permeability cases were explored but only the most representative cases, namely the cases with permeability, k, being 6.6×10^{-5} m/s, 6.6×10^{-4} m/s, 6.6×10^{-3} m/s and 6.6×10^{-2} m/s, are shown.

Figure 3.5 shows the free-field displacement time histories at 0.5 m depth intervals, for the above mentioned permeability cases. Conversely to Figure 2.15, Figure 3.5 shows that the free-field displacement was lower for cases with permeability higher than 6.6×10^{-4} m/s (10 times greater than the benchmark case and it appears that this case overlaps the benchmark case, $k = 6.6 \times 10^{-5}$ m/s). However, Figure 3.6, which shows the free-field displacement profile at 10 seconds of shaking, shows more clearly that at 10 seconds, the soil with permeability $k = 6.6 \times 10^{-4}$ m/s displaces more than the benchmark case for the upper 3.5 m of the soil stratum.

Figure 3.7, shows the variation in flexible and stiff pile head displacements pertaining to the four different permeability cases. Similarly to the observation made from

Figure 2.17, Figure 3.7 shows pile head displacement decreased with increasing permeability.

Free-field excess pore pressures for the four different permeability cases are shown in Figure 3.8. Behavior similar to that from Figure 2.18 is observed. The pore pressure build up was less for higher permeability cases to the extent that the soil case with the highest permeability, $k = 6.6x10^{-2}$ m/s, did not reach liquefaction throughout the entire soil stratum. The case with next highest permeability, $k = 6.6x10^{-3}$ m/s did not liquefy for depths of about 2.5 m and greater.

Figure 3.9 and Figure 3.10 compare the pore pressure time history response near the stiff pile, on the upslope side and downslope side respectively, for the different permeability cases. It was observed that cycle-by-cycle dilation is reduced with increasing permeability.

Similarly, Figure 3.11 and Figure 3.12 compare the pore pressure time history response near the flexible pile, on the upslope side and downslope side respectively, for the different permeability cases. Cycle-by-cycle dilation is also observed to decrease with increasing permeability.

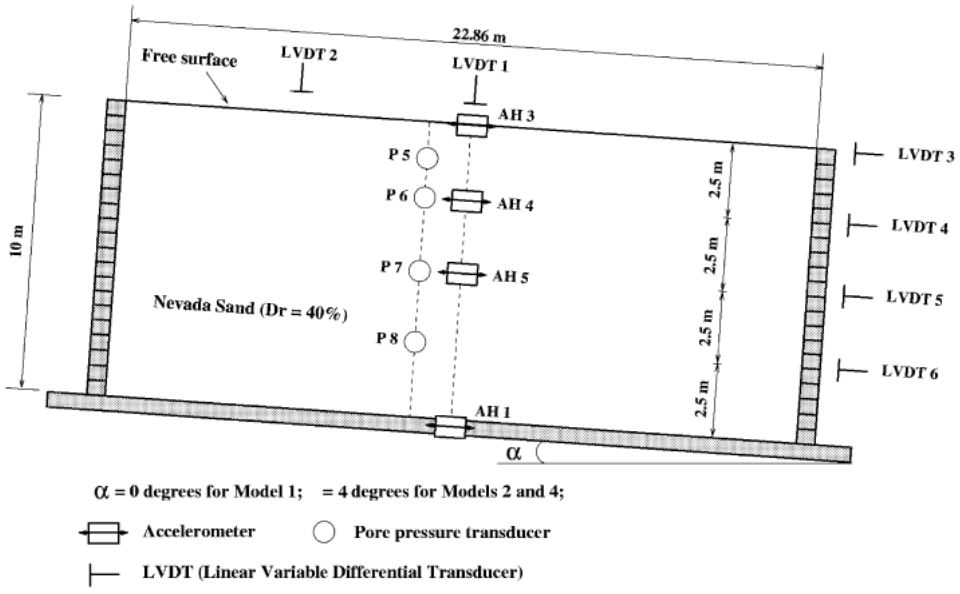

Figure 3.1. Velacs Model 2 Setup and Instrumentation (Taboada 1995)

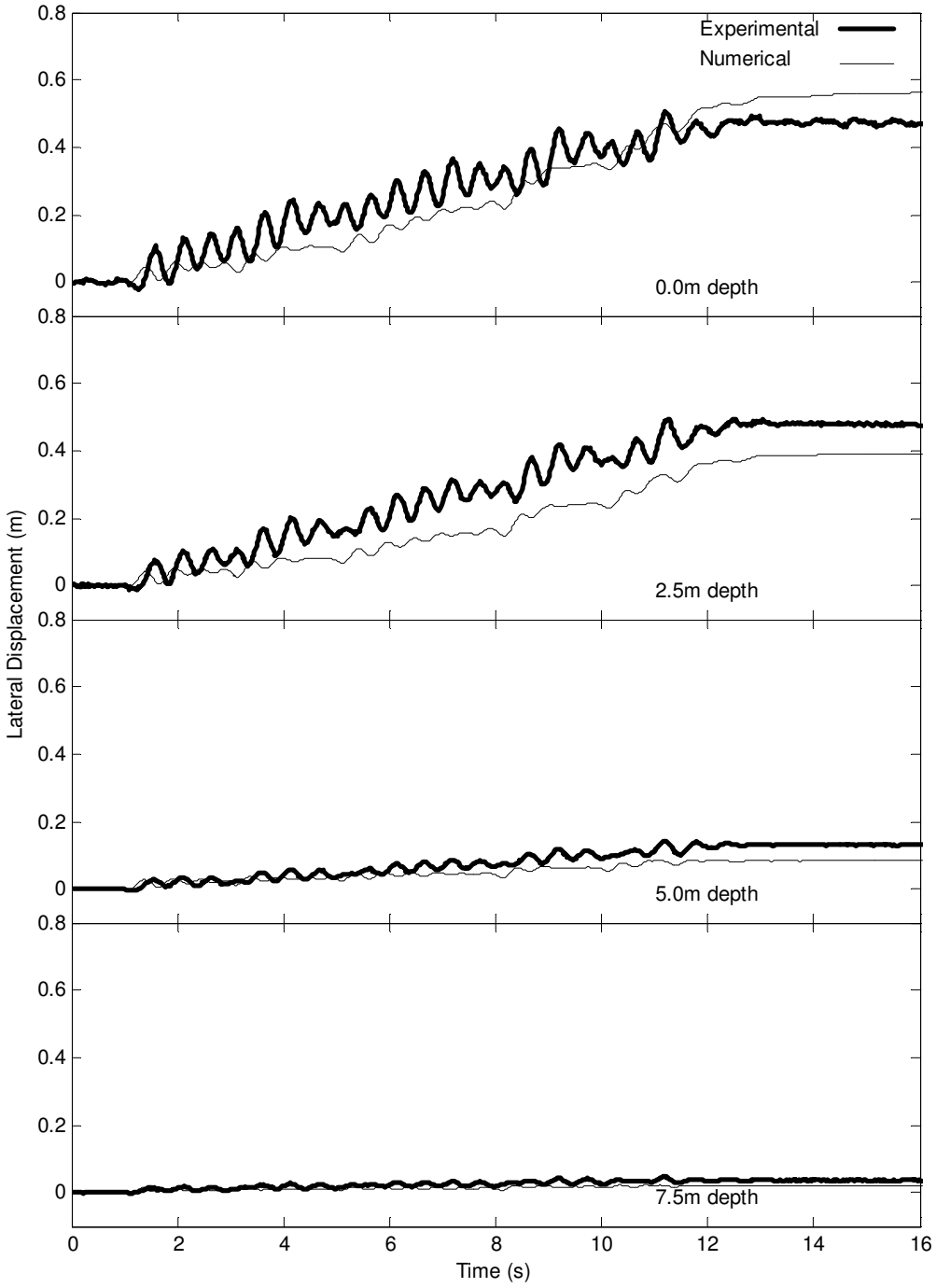

Figure 3.2. Velacs Model 2 Recorded and computed lateral displacement

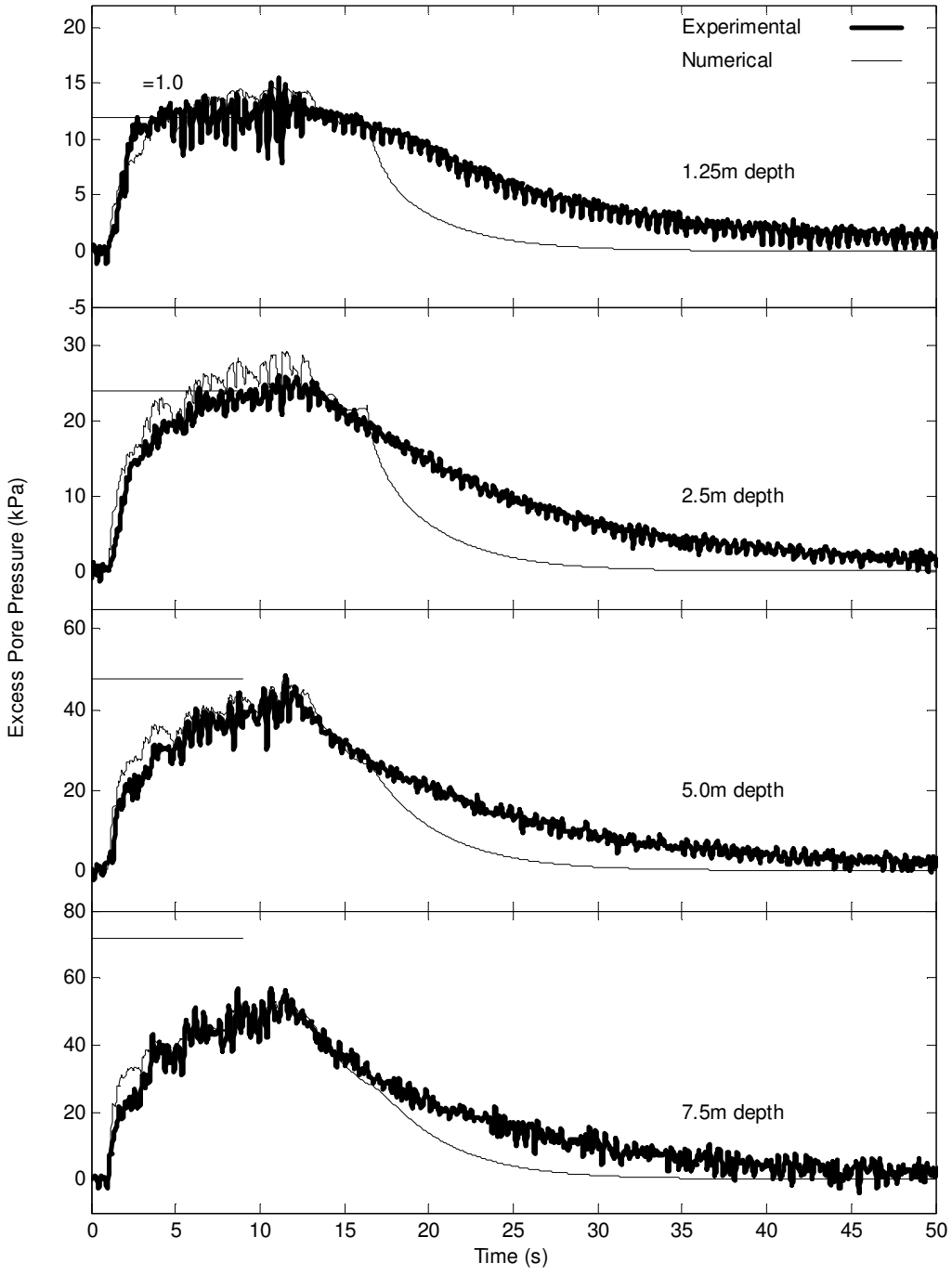

Figure 3.3. Velacs Model 2 Recorded and computed excess pore pressures

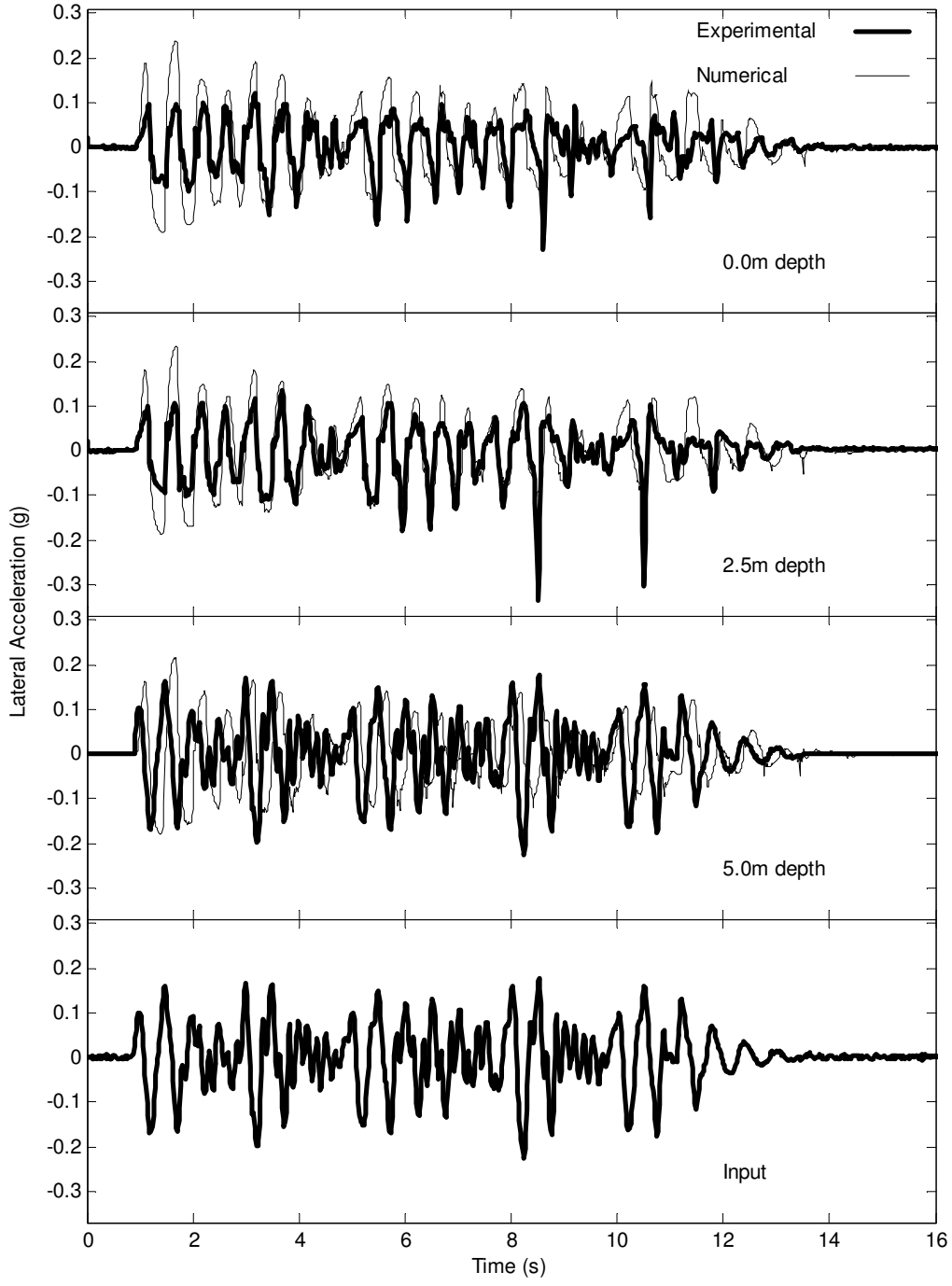

Figure 3.4. Velacs Model 2 Recorded and computed lateral accelerations

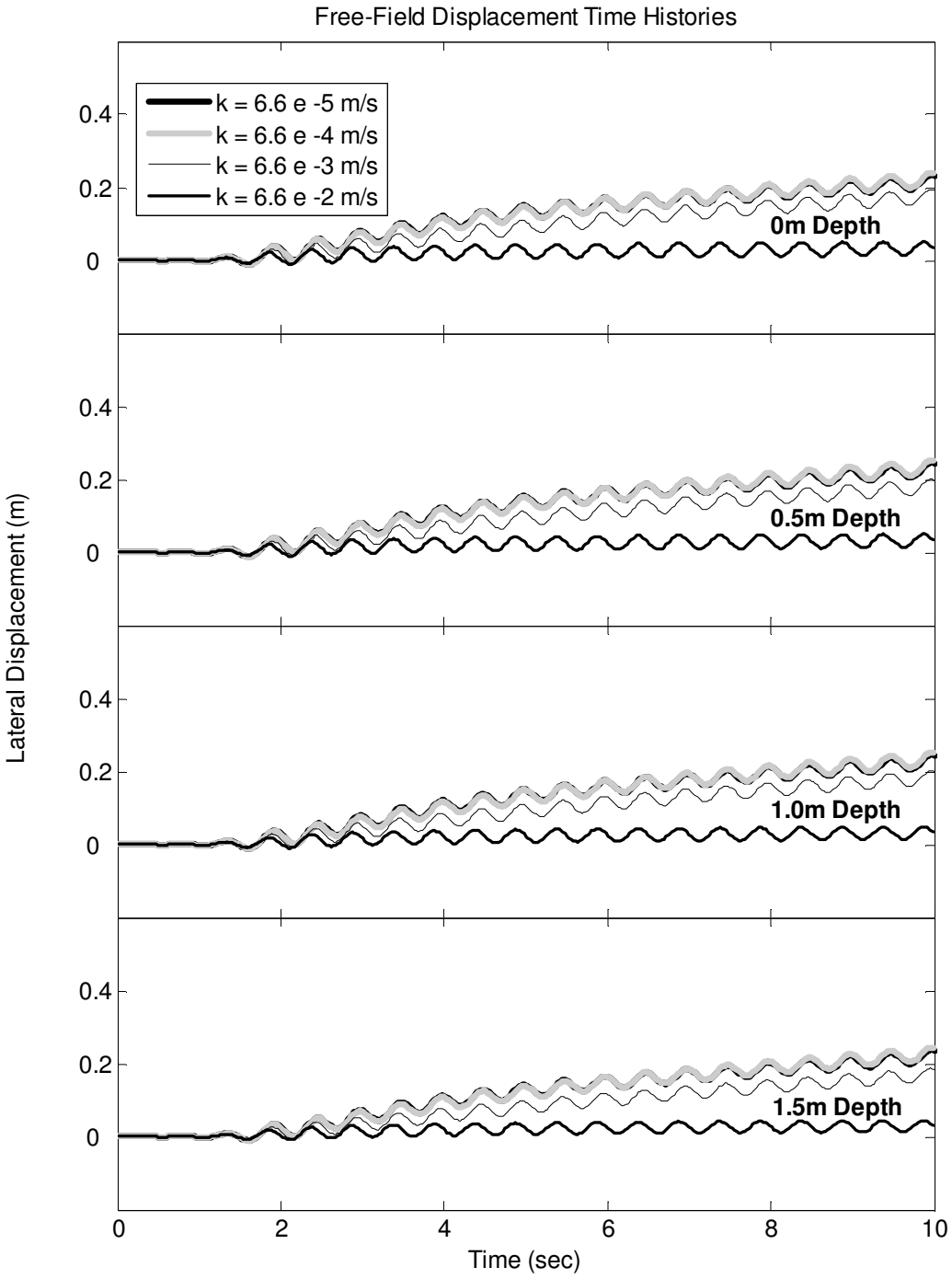

Figure 3.5. Influence of permeability on free-field displacements, Velacs sand

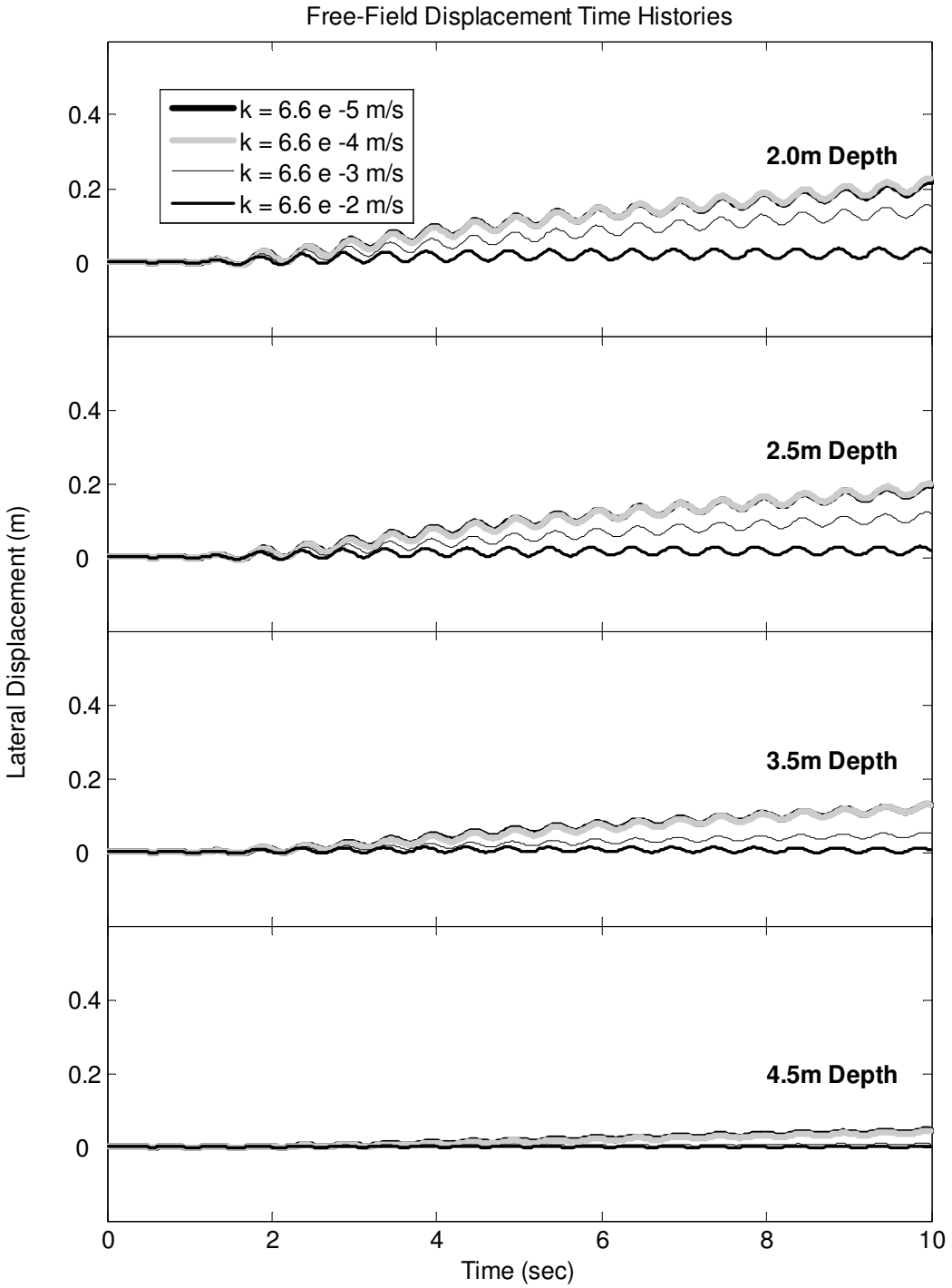

Figure 3.5. Influence of permeability on free-field displacements, Velacs sand(cont'd)

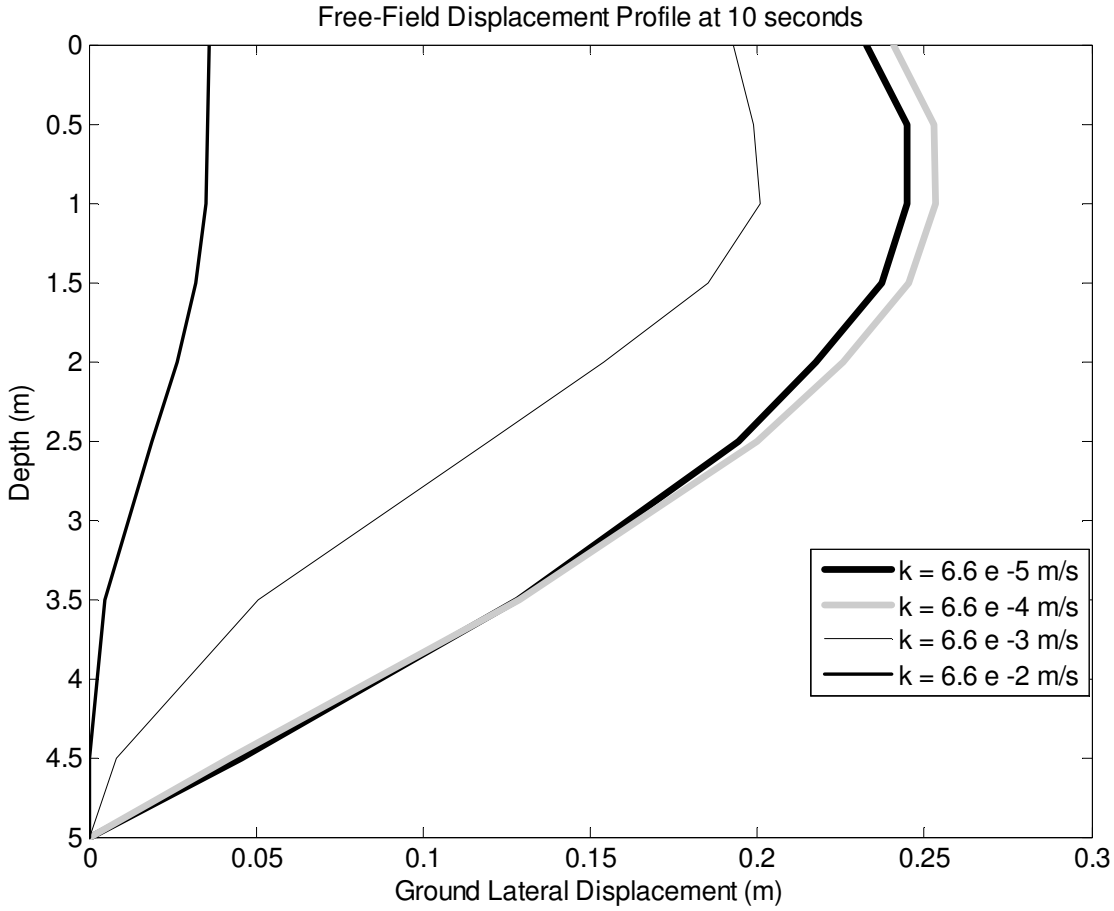

Figure 3.6. Influence of permeability on free-field displacement profile at 10 seconds, Velacs sand representative cases

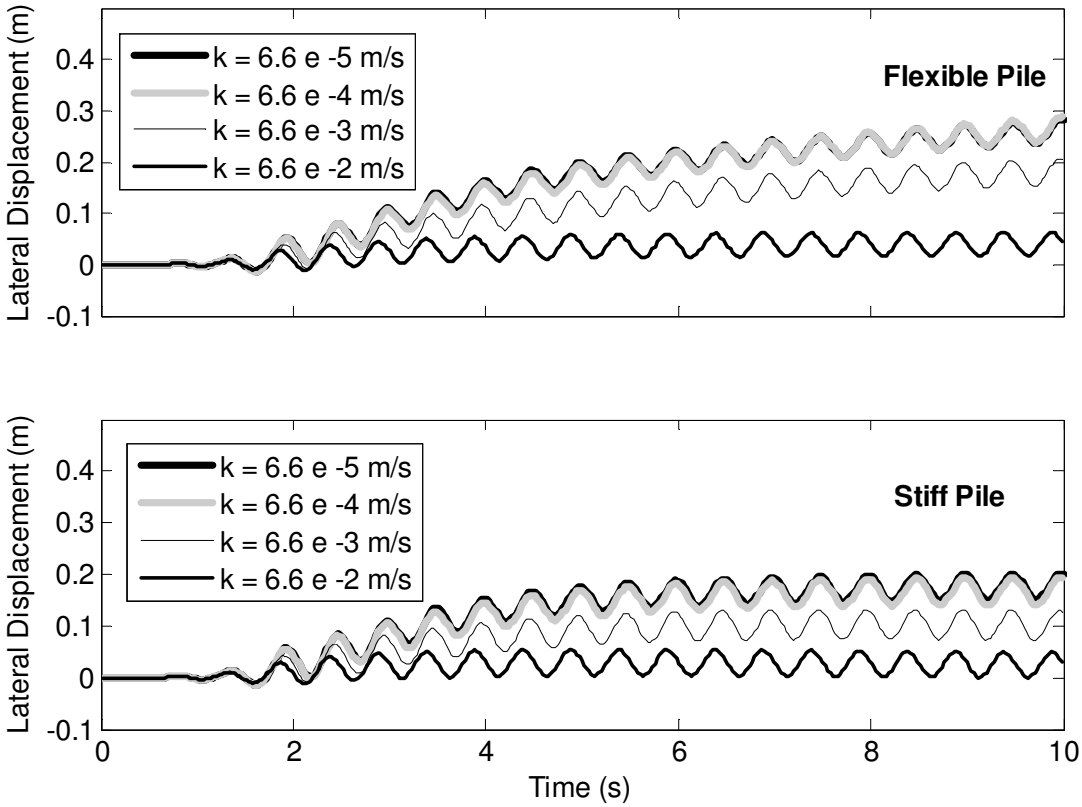

Figure 3.7. Influence of permeability on pile head displacements, Velacs sand

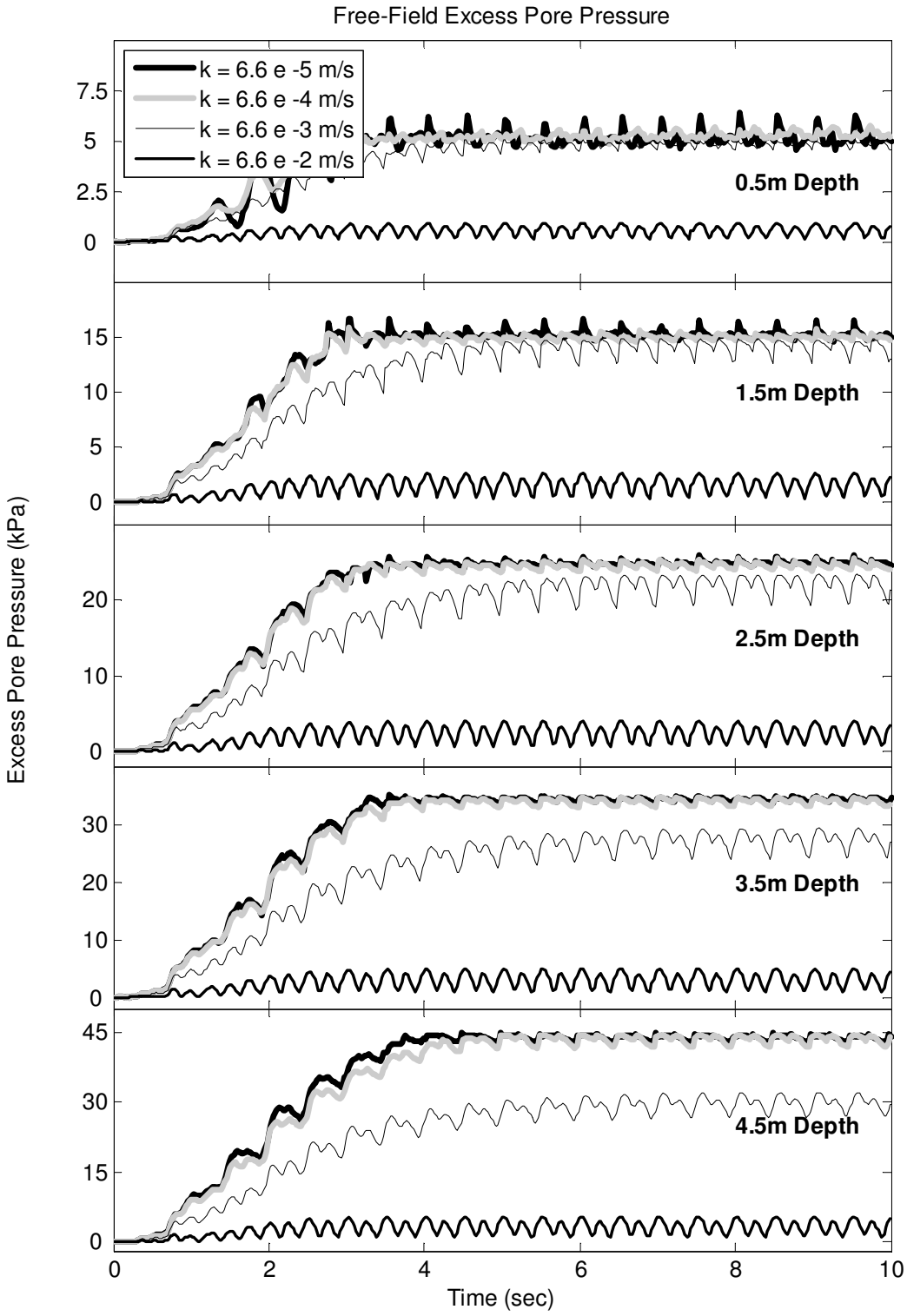

Figure 3.8. Influence of permeability on free-field excess pore pressures, Velacs sand

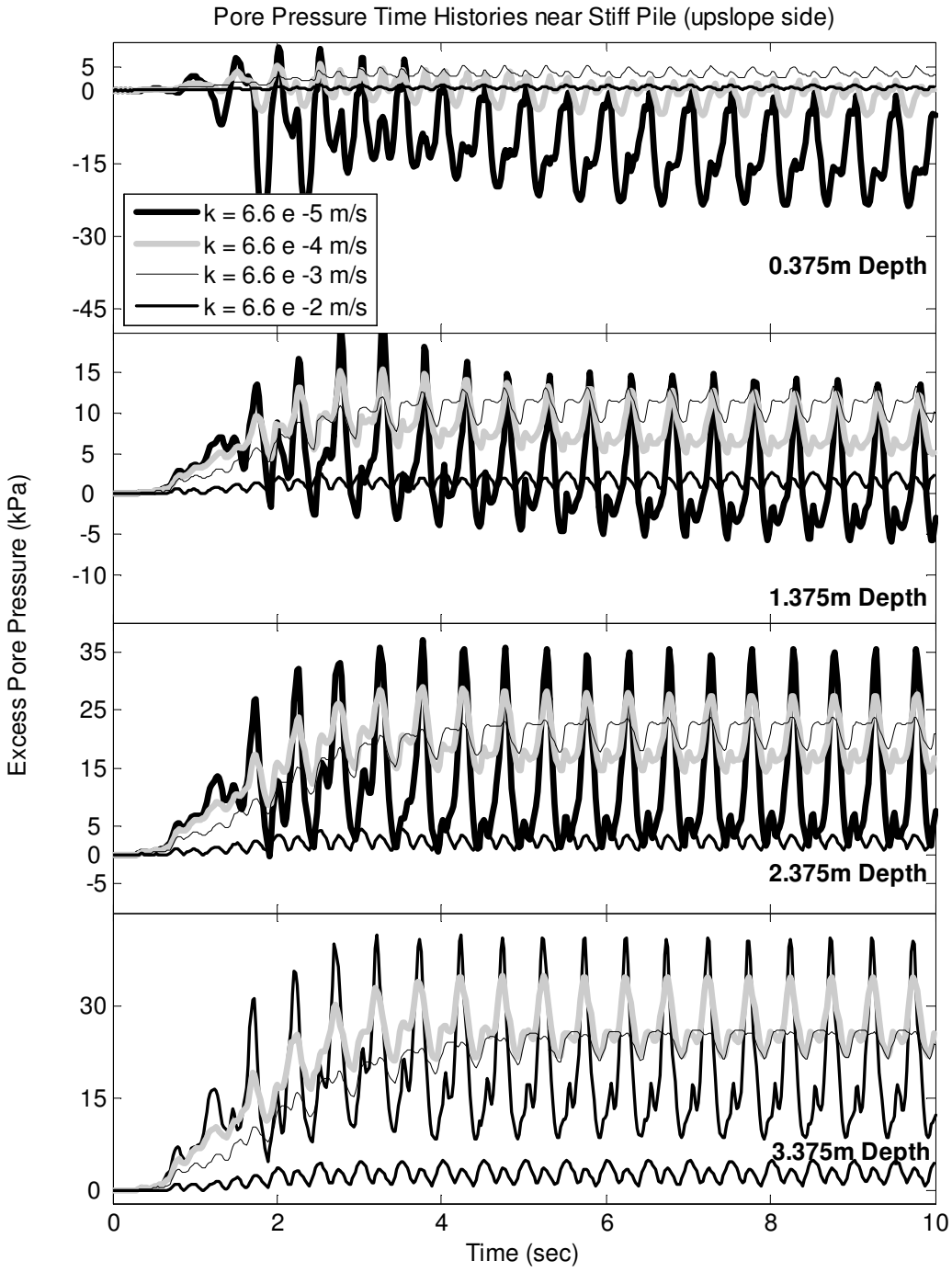

Figure 3.9. Influence of permeability on
pore pressures time histories near stiff pile (upslope side), Velacs sand

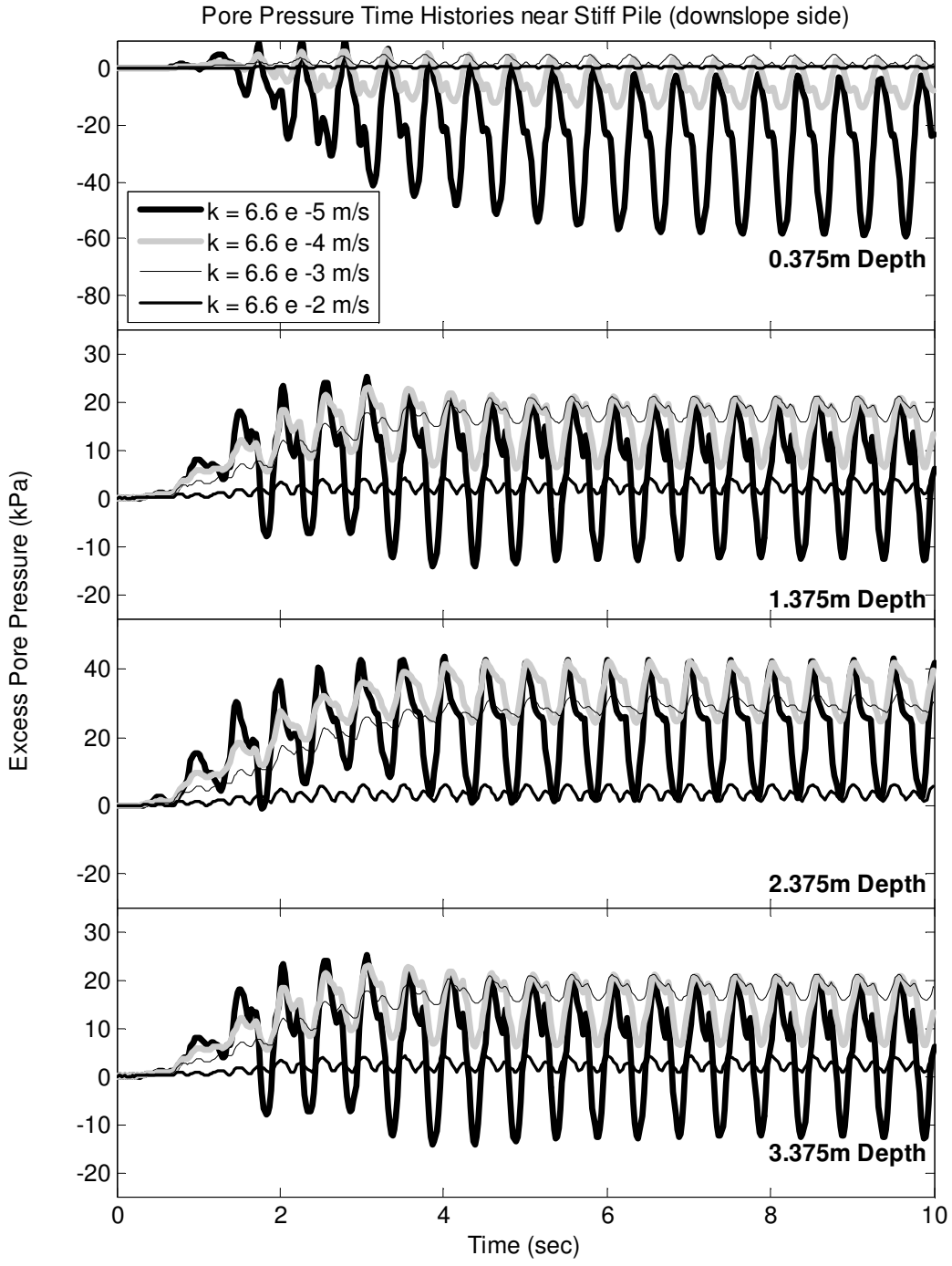

Figure 3.10. Influence of permeability on
pore pressures time histories near stiff pile (downslope side), Velacs sand

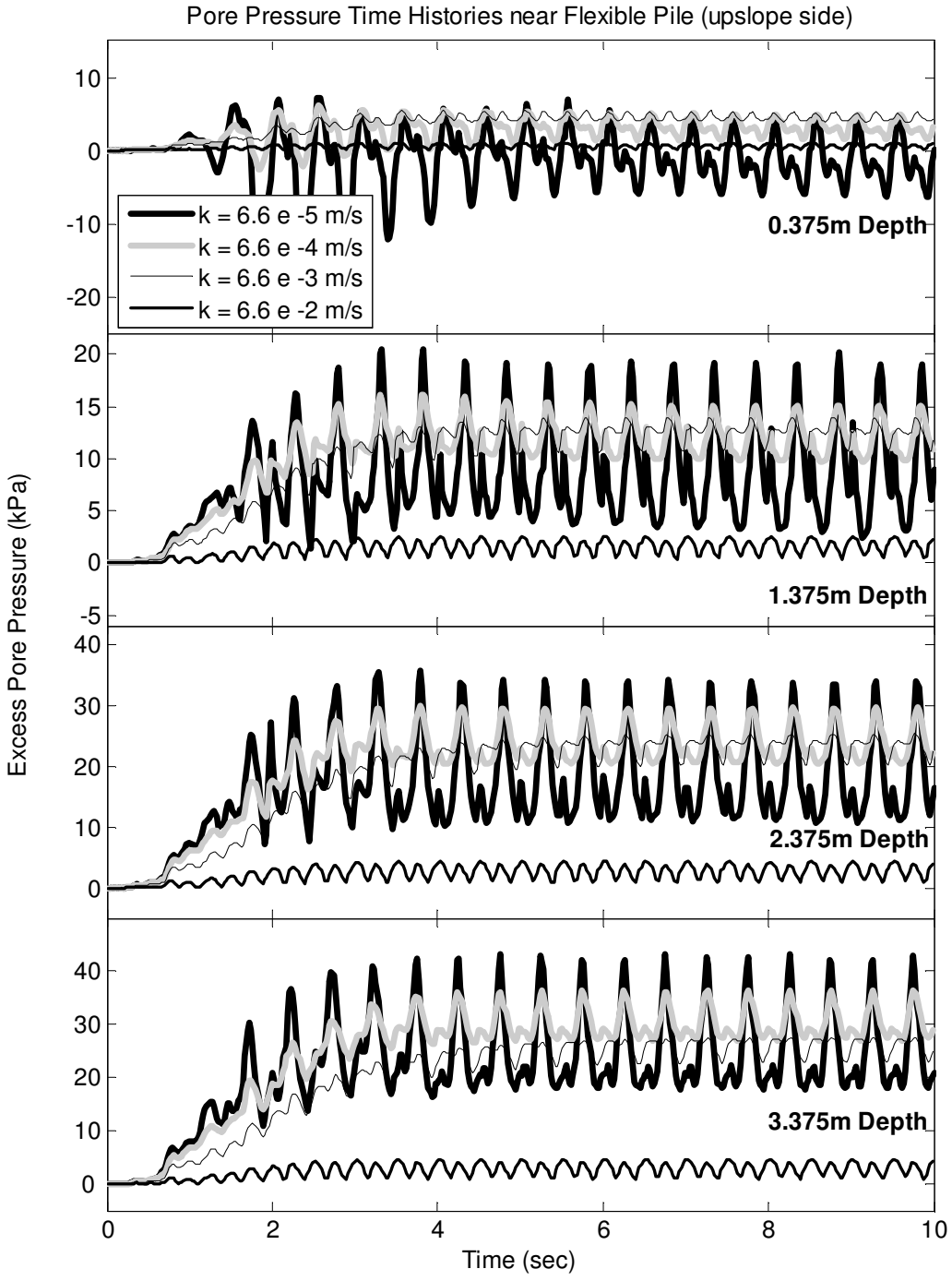

Figure 3.11. Influence of permeability on
pore pressures time histories near flexible pile (upslope side), Velacs sand

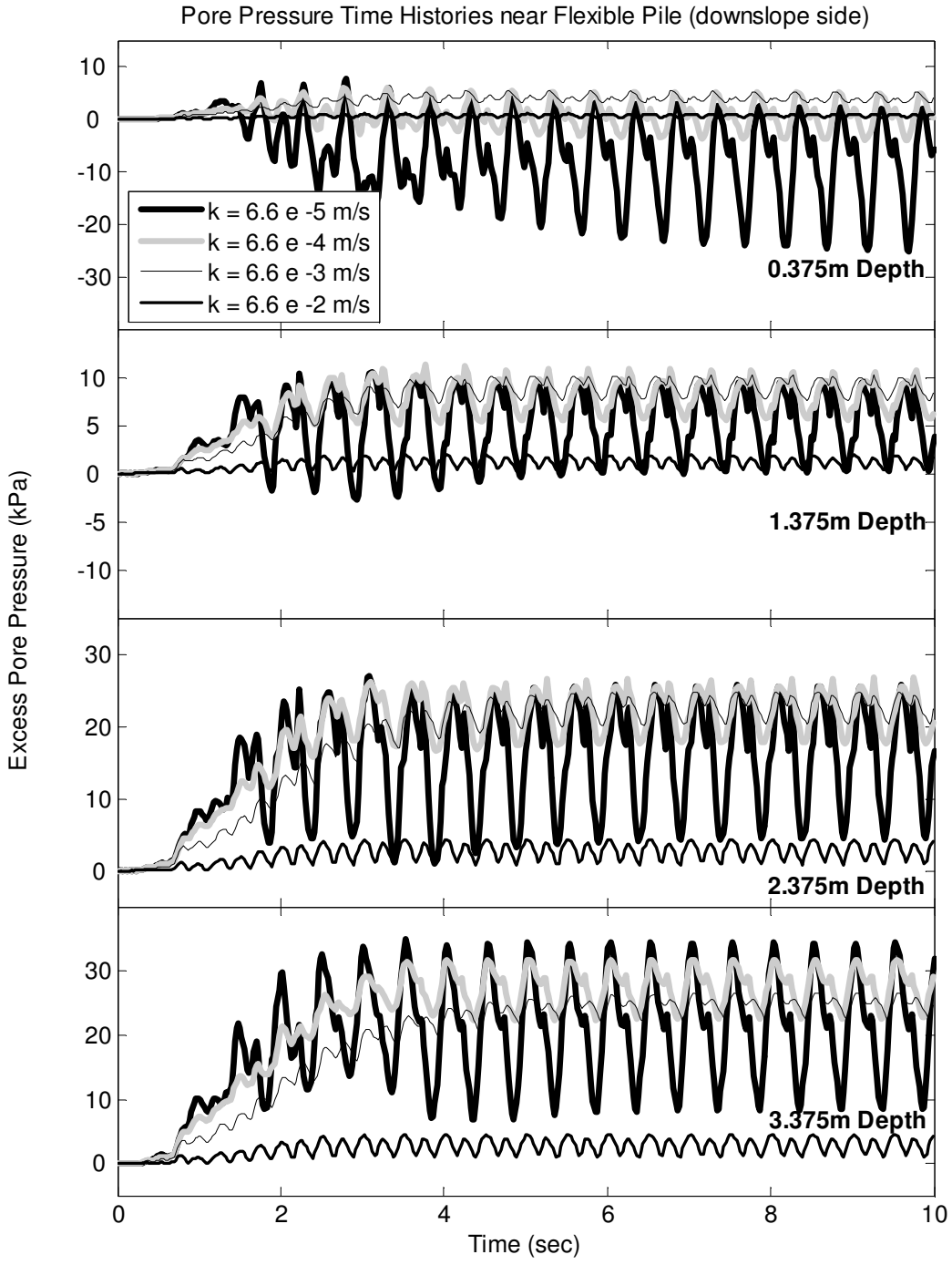

Figure 3.12. Influence of permeability on
pore pressures time histories near flexible pile (downslope side), Velacs sand

APPENDIX 3.1: Additional Figures for Chapter 3

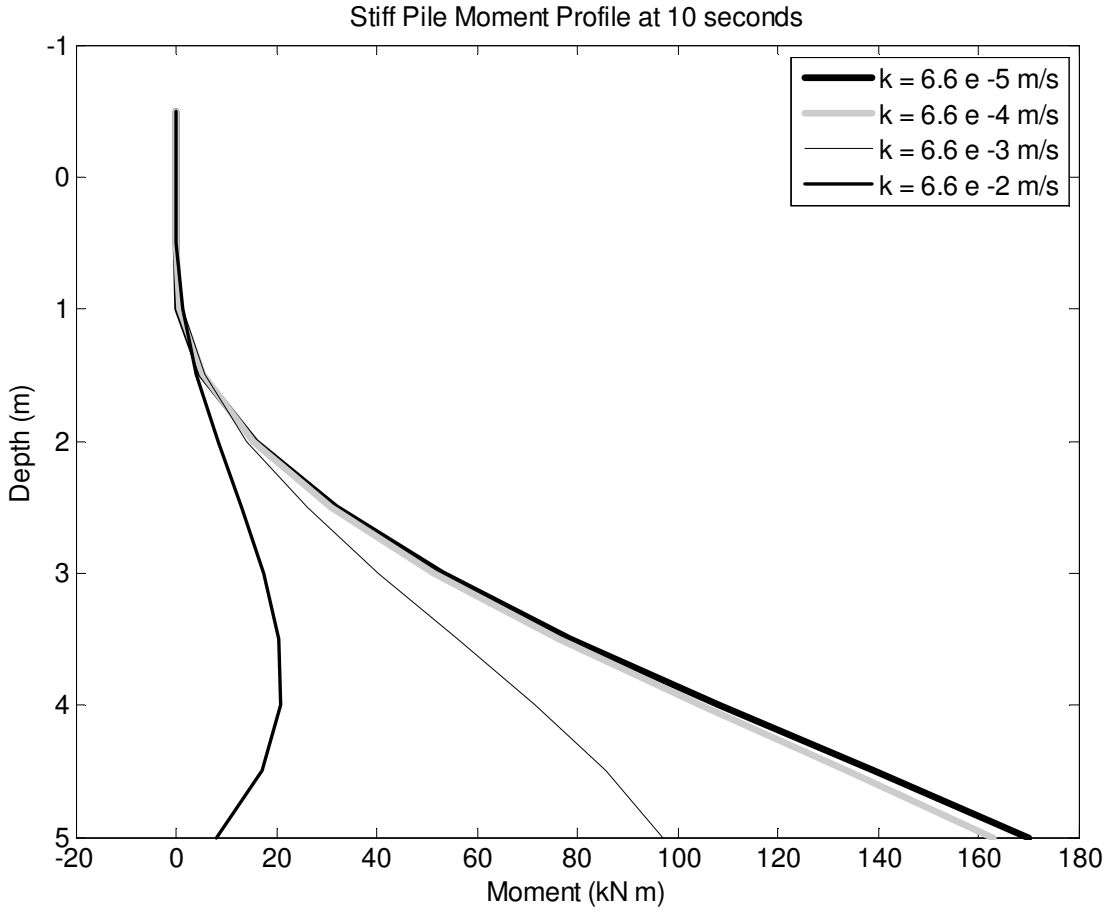

Figure 3.13. Influence of permeability on stiff pile moment profile at 10 seconds, Velacs sand

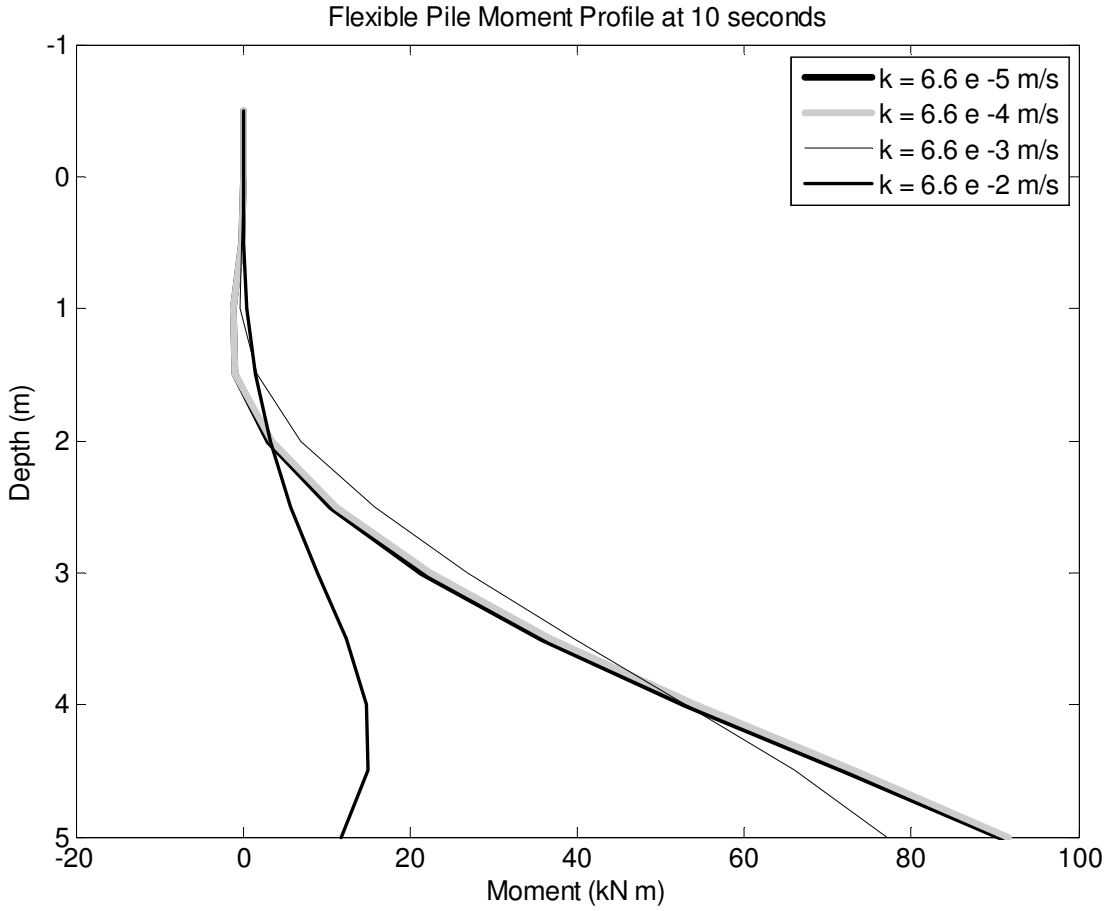

Figure 3.14. Influence of permeability on
flexible pile moment profile at 10 seconds, Velacs sand

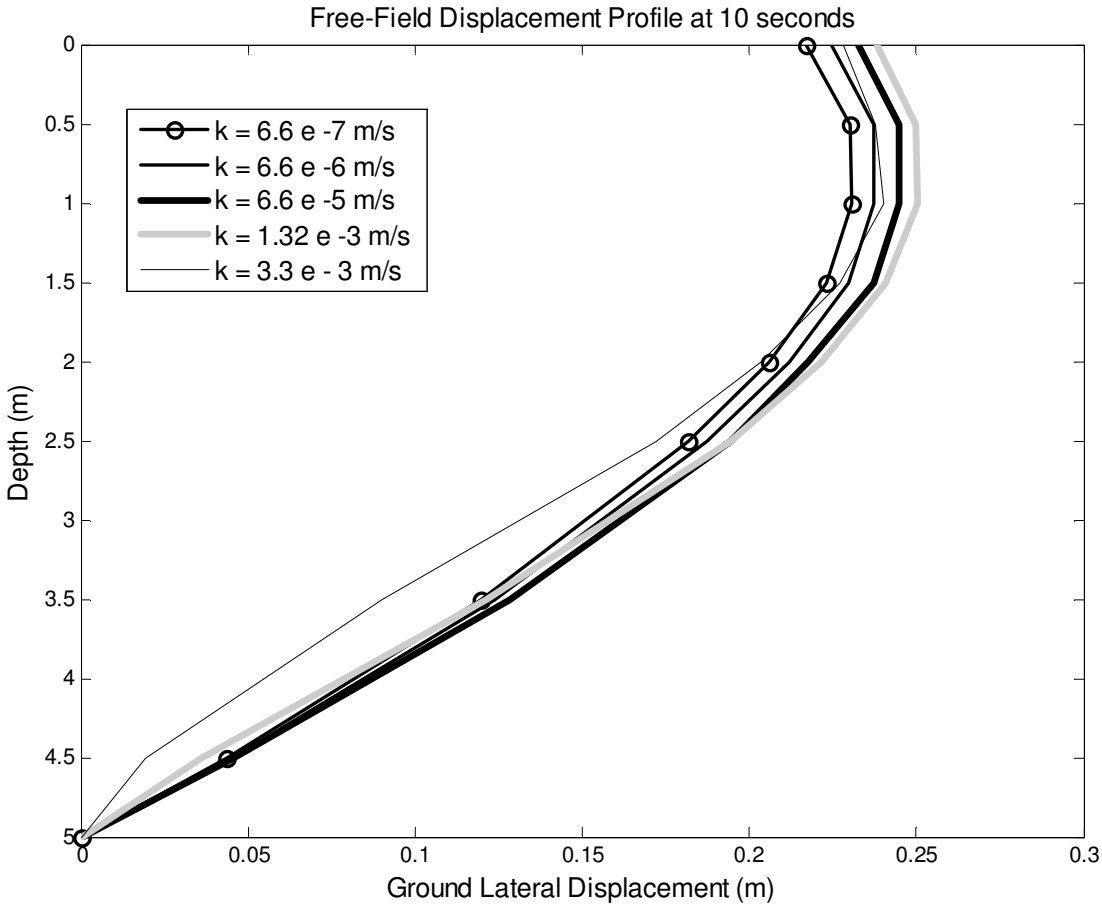

Figure 3.15. Influence of permeability on free-field displacement profile at 10 seconds, Velacs sand (all permeability cases)

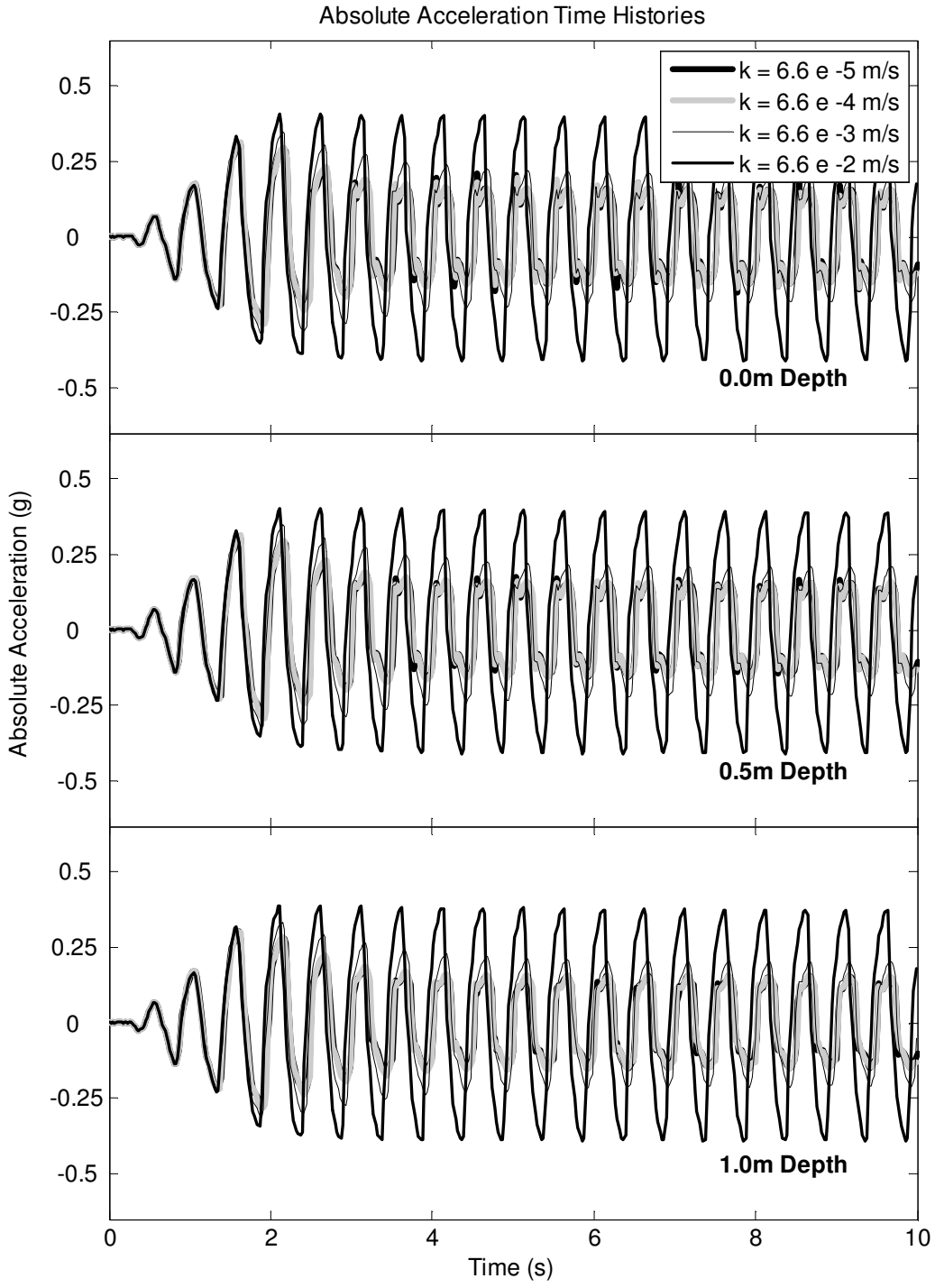

Figure 3.16. Influence of permeability on
free-field acceleration time histories, Velacs sand

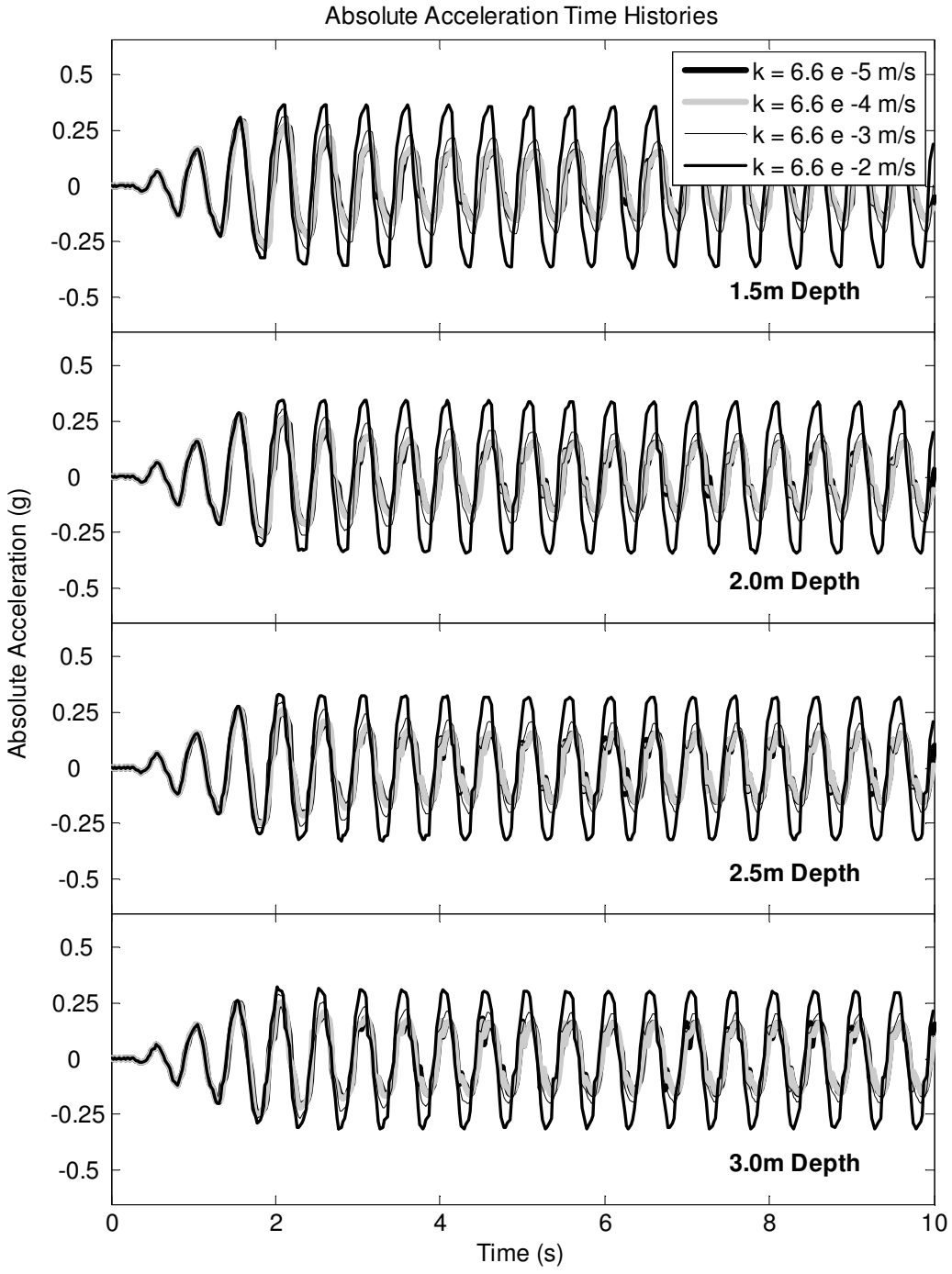

Figure 3.16. Influence of permeability on
free-field acceleration time histories, Velacs sand (cont'd)

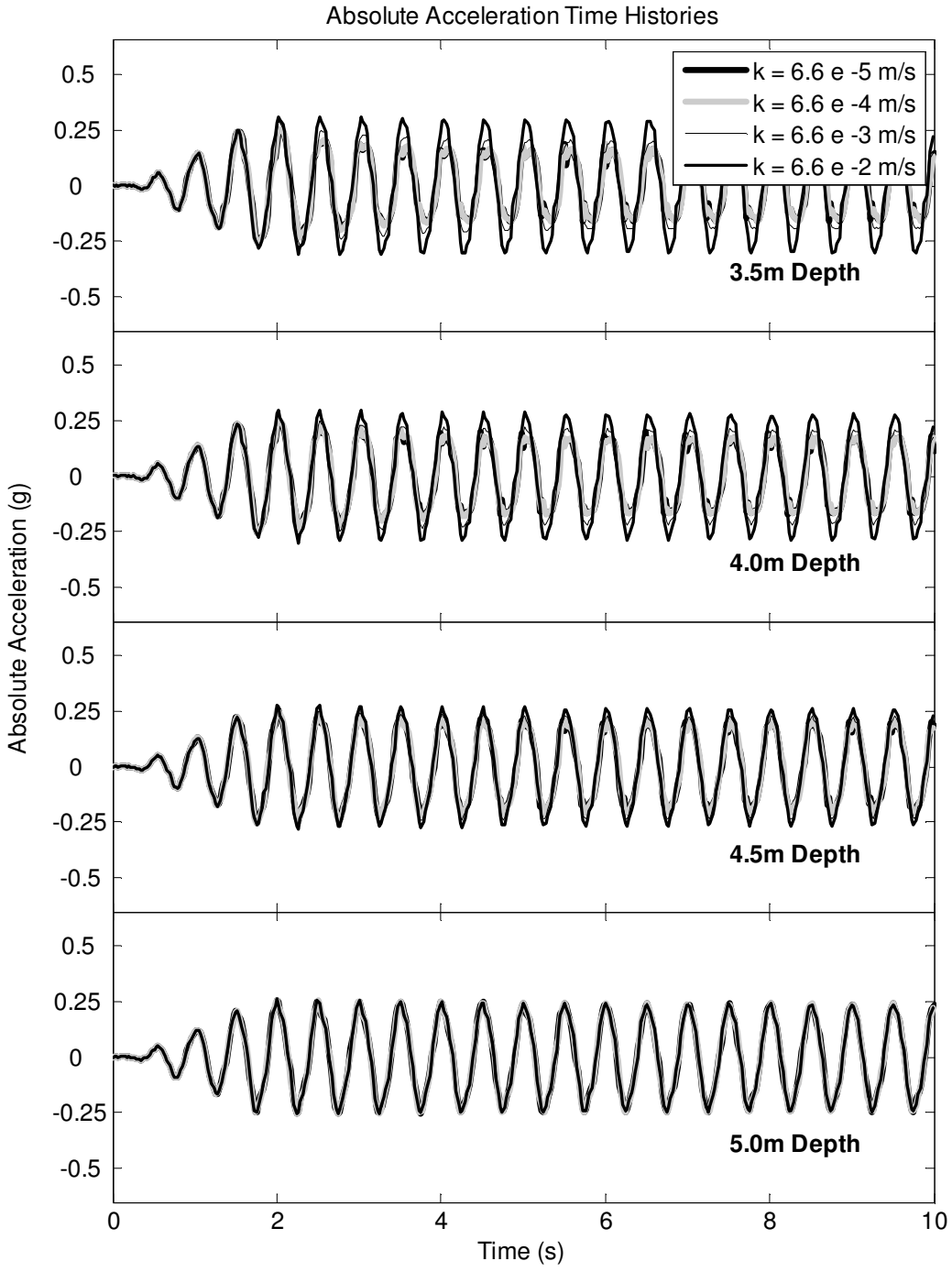

Figure 3.16. Influence of permeability on
free-field acceleration time histories, Velacs sand (cont'd)

CHAPTER 4

CONCLUDING REMARKS

4.1 Summary and Highlights of Findings

The efforts presented in this study are based on a numerical investigation with an extensively calibrated FE model. The model was calibrated simulating a shake table experiment conducted in Japan, namely Japan4 (He 2005). The permeability was then increased and decreased and its effects on the soil and piles were explored. Data from a centrifuge experiment, namely VELACS Model 2 (Taboada 1995), was also used to explore the effects permeability has on the soil and piles. The purpose for this second analysis was to investigate the permeability effects using a sand type that exhibits a more noticeable tendency for dilation.

The main findings were mostly similar for both investigations. It was found that increasing soil permeability weakens soil dilation and that if permeability becomes too high, pore pressure buildup is significantly reduced. For the sand with less dilative tendency, it was observed that the accumulated lateral soil displacement increased with increasing permeability until the permeability was increased to the point were the soil did not liquefy, thus decreasing the lateral displacement. A similar behavior was observed for the sand with higher dilative tendency except that its dilative characteristic produced a higher effective confinement (during the phases of dilation tendency), which allowed it to more readily preclude liquefaction (resulting in less displacement as permeability increased). Furthermore, it was found that pile head displacement decreased with increasing permeability. It is worthy to mention

however, that for the sand with a less dilative tendency, the pile head displacement decreased with increasing permeability because even though the soil displacement increased, with increasing permeability its confinement decreased more and more (during the dilative tendency phases) and became more readily able to displace around the pile (thus imposing lower load on the piles). As described above, for the sand with a more dilative tendency, the soil itself displaced less as permeability was increased, thus imposing lower load on the piles (and less pile displacement).

REFERENCES

Abdoun, T., Dobry, R., O'Rourke, T. D., and Goh, S. H. (2003). "Pile response to lateral spreads: Centrifuge modeling," *Journal of Geotechnical and Geoenvironmental Engineering*. 129(10), Oct., 869-878.

Arulmoli, K., Muraleetharan, K. K., Hossain, M. M., and Fruth, L. S. (1992). "VELACS: Verification of liquefaction analyses by centrifuge studies, laboratory testing program, soil data report," Report, The Earth Technology Corporation, Project No. 90-0562, Irvine, CA.

Biot, M. A. (1962). "The mechanics of deformation and acoustic propagation in porous media," *Journal of Applied Physics*, 33(4), 1482-1498.

Dobry, R., Taboada, V. and Liu, L. (1995). "Centrifuge modeling of liquefaction effects during earthquakes," *Proc. 1st Intl. Conf. On Earthquake Geotechnical Engineering*, IS Tokyo, K. Ishihara, Tokyo, Japan, Nov. 14-16, 1291-1324.

Dobry, R. and Abdoun. T. (1998). "Post-triggering response of liquefied sand in the free field and near foundations," *Proceedings of Geotechnical Earthquake Engineering and Soil Dynamics III*, Dakoulas, P., Yegian, M. and Holtz, R. D., Eds., Seattle, Washington, Aug 3-6, 270-300.

Dobry, R., Abdoun, T., O'Rourke, T. D., and Goh, S. H. (2003). "Single piles in lateral spreads: Field Bending Moment Evaluation," *Journal of Geotechnical and Geoenvironmental Engineering*, 129(10), Oct., 879-889.

Elgamal, A., Yang, Z., Parra, E., and Ragheb, A. (2003). "Modeling of Cyclic Mobility in Saturated Cohesionless Soils," *International Journal of Plasticity*, 19(6), 883-905.

Elgamal, A. (2008). "Personal Communications".

He, L. (2005). Liquefaction-Induced Lateral Spreading and its Effects on Pile Foundations, *Ph.D. Thesis,* Dept. of Structural Engineering, University of California, San Diego, La Jolla, California.

He, L., Elgamal, A., Abdoun, T., Abe, A., Dobry, R., Meneses, J., Sato, M., and Tokimatsu, K. (2006). "Lateral load on piles due to liquefaction-induced lateral spreading during one-g shake table experiments," *Proc., 8th U.S. National Conference on Earthquake Engineering,* April 18-22, 2006, San Francisco, California, USA, Paper No. 895.

Hill, R. (1950). The mathematical theory of plasticity, Oxford University Press, London.

Iai, S. (1991). "A strain space multiple mechanism model for cyclic behavior of sand and its application," Earthquake Engineering Research Note No. 43, Port and Harbor Research Institute, Ministry of Transport, Japan.

Ishihara, K. (1985). "Stability of natural deposits during earthquakes," *Proceedings of the 11th International Conference on Soil Mech. Foundation Engineering*., Balkema, Rotterdam, 321-276.

Iwan, W. D. (1967). "On a class of models for the yielding behavior of continuous and composite systems," *Journal of Applied Mechanics*, ASME 34, 612-617.

Kramer, S. L. (1996). Geotechnical earthquake engineering, Prentice Hall, Upper Saddle River, NJ.

Law, K. H. and Mackay, D. R. (1993). "A parallel row-oriented sparse solution method for finite element structural analysis," *International Journal for Numerical Methods in Engineering*, 36(17), 2895-2919.

Mackay, D. R. (1992). "Solution methods for static and dynamic structural analysis on distributed memory computers," *Ph.D. Thesis*, Stanford University.

Mroz, Z. (1967). "On the description of anisotropic work hardening," *J. Mechanics and Physics of Solids*, 15, 163-175.

Parra, E. (1996). "Numerical modeling of liquefaction and lateral ground deformation including cyclic mobility and dilation response in soil systems," *Ph.D. Thesis*, Rensselaer Polytechnic Institute, Troy, NY.

Peng, J. (2002). "An Internet-enabled software framework for the collaborative development of a structural analysis program," *Ph.D. Thesis*, Department of Civil and Environmental Engineering, Stanford University, Stanford, CA.

Prevost, J. H. (1985). "A simple plasticity theory for frictional cohesionless soils," *Soil Dynamics and Earthquake Engineering*, 4(1), 9-17.

Taboada, V. M. (1995). "Centrifuge modeling of earthquake-induced lateral spreading in sand using a laminar box," *PhD Thesis*, Civil Engineering Dept., Rensselaer Polytechnic Institute, Troy, N.Y.

Vaid, Y. P. and Thomas, J. (1995). "Liquefaction and post liquefaction behavior of sand," *Journal of Geotechnical Engineering*, ASCE 121(2), 163-173.

Vaid, Y.P. and Sivathayalan, S.. (1999). "Fundamental factors affecting liquefaction susceptibility of sands." Physics and mechanics of soil liquefaction, P. Lade and J. Yamamuro, eds., Balkema, Rotterdam, 105-120.

Yang, Z. (2000). "Numerical modeling of earthquake site response including dilation and liquefaction," *Ph.D. Thesis*, Columbia University, New York, NY.

Yang, Z. and Elgamal, A. (2003). "Application of unconstrained optimization and sensitivity analysis to calibration of a soil constitutive model," *International Journal for Numerical and Analytical Methods in Geomechanics*, 27(15), 1255-1316.

Yang, Z., Elgamal, A., and Parra, E. (2003). "A computational model for cyclic mobility and associated shear deformation," *Journal of Geotechnical and Geoenvironmental Engineering*, 129(12), 1119-1127.